Laser Surface Treatment for Targeted Strengthening of Metallic Multilayer Thin Films

Melicent Stossel

A dissertation

submitted in partial fulfillment of the

requirements for the degree of

Doctor of Philosophy

University of Washington

2024

Reading Committee:

Junlan Wang, Chair

Xu Chen

Lucas Meza

Program Authorized to Offer Degree:

Mechanical Engineering

University of Washington

Abstract

Laser Surface Treatment for Targeted Strengthening of Metallic Multilayer Thin Films

Melicent Stossel

Chair of the Supervisory Committee:

Junlan Wang

Department of Mechanical Engineering

In this dissertation, pulsed laser surface treatment is applied to two multilayer thin film material systems, Ti/Ni and Cu/Al, to locally strengthen the surface layers of a multilayer film while preserving the original structure and properties of the base layers. Picosecond laser surface treatment was applied to Ti/Ni to investigate the effect of laser pulse energy, individual layer thickness, and total film thickness on the surface strengthening. Intermetallic phase precipitation was shown to be a dominant mechanism for laser-induced strengthening of the Ti/Ni multilayer. Therefore, Cu/Al, a material with a plethora of potential intermetallic phases, was treated with nano- and picosecond pulse lasers to generate intermetallic phases with the goal of confined

surface strengthening. The laser surface treatment method was then applied as an array to optimize the laser treatment parameters for scaling to industrial applications.

Picosecond pulsed laser treatment of Ti/Ni showed that for increasing laser pulse energy, the multilayer cross-section initially consists of a clear multilayer structure, followed by the onset of an intermixed layer at the film surface that grows in thickness as energy increases until the film is fully intermixed. Intermixing was not sufficient to cause surface strengthening, instead there was an increase in hardness after intermetallic phases were generated at higher pulse energy. The effect of individual layer thickness was compared between 20 nm and 50 nm layers, and the results showed that the formation of an intermixed layer and the onset of intermetallic phase precipitation required less energy for larger layers. Incorporating the effect of a 500 nm and 1 μm total film thickness shows more energy is required to generate the intermixed layer and reach the critical energy to form intermetallic phases for thicker Ti/Ni films.

Initial testing of the Cu/Al multilayer system revealed a reflectivity of over 90% when treated with light at 1064 nm, necessitating the addition of a 25 nm Ti capping layer to improve absorption of the incident energy. Nanosecond and picosecond pulsed laser treatments were applied to the Cu/Al + Ti multilayer films to generate intermetallic phases and measure the corresponding increase in hardness. Surface treatment with the nanosecond laser resulted in a smooth, microcracked surface with no intermixed layer but a dramatic increase in hardness to a maximum of over 10 GPa for nanoindentation at shallow contact depth that decreases to the as-deposited hardness of around 4 GPa with increasing contact depth. Picosecond laser treatment results in the formation of a highly textured surface and an intermixed layer with clear intermetallic phase generation, however the resulting strengthening is generally limited to 5-7 GPa over a range of shallow contact depths.

Picosecond laser treatment was applied in a hexagonal array pattern to extend the treatment from a single location test to an area treatment. Arrays were created with 0% shot overlap as well as 50% shot overlap in x and y directions. Both single-pulse arrays and multiple pulse arrays were generated, with an emphasis on developing single-pulse arrays that show clear intermetallic phase generation and a corresponding increase in hardness to avoid complications associated with multi-pulse testing such as thermal accumulation.

Table of Contents

List of Figures

List of Tables

Dedication

To my family

Acknowledgements

I would like to acknowledge the financial support provided by the University of Washington Department of Mechanical Engineering, the Clean Energy Institute, the Boeing Company, and the Joint Center for Aerospace Technology Innovation during various stages of my Ph.D. study.

I would like to express my deepest gratitude to my advisor, Professor Junlan Wang. Her support, patience, and guidance over the many years we have worked together have been invaluable and allowed me to pursue a wide range of opportunities while I worked toward my Ph.D.

I would like to thank Professor Lucas Meza, Professor Xu Chen, and Professor Dwayne Arola for serving on my supervisory committee.

I would like to thank all my previous labmates for the feedback and knowledge shared in group meetings, and in particular, Dr. Zhou Yang and Dr. Yang Zhou whose work in thermal strengthening of Ti/Ni and Cu/Al is the precursor and bedrock of this project, and Dr. Phillip Miller who trained me to operate the lasers and design optics experiments. I am grateful to my current labmates, Kris Gill, Allen Kim, and Peyton Clark, for their thoughtful feedback, questions, and suggestions that have helped me see my research from new perspectives.

Finally, I am eternally grateful for the love and support of my family and friends.

1. Introduction

Nanolaminate materials have attracted great interest in research and industry due to their superior functional properties, and particularly the mechanical strength as compared to monolithic films of the component materials. Annealing nanolaminate materials has been demonstrated for a range of material systems as a method of achieving ultrahard materials, beyond the strengthening inherent in the layer thickness effect. However, depending on the annealing temperature, a variety of thermal processes could take place, such as atomic diffusion, intermixing, recrystallization, grain growth, phase transformations, and intermetallic precipitations. There are cases where annealing is not desirable and could result in decreased strength, morphological instability, oxidation, or thermal instability [1, 2]. Additionally, the focus on developing ultra-strength nanolaminate materials does so at the detriment of other desirable properties, such as ductility and fracture toughness. For applications where a combination of strength and ductility is desired, a more targeted strengthening would allow for tailoring material properties to suit the specific application. Gradient materials are one solution to tailored material properties that optimize mechanical properties and performance. Gradient nanostructured metals and alloys have exhibited unique combinations of mechanical properties, including strength-ductility synergy, superior work hardening and fatigue properties, and improved resistance to wear, corrosion, and friction [3]. Through structural gradients like grain size, twinning, and lamellar thickness, or chemical gradients including phase distribution, solid-solution concentration, and chemical components, there is a lot of flexibility in designing nanolaminate materials to accomplish specific goals. Alternatively, targeted modification of nanolaminate materials is also possible through laser surface treatment. The advantages of laser surface modification include the wide applicability across bulk and thin film materials of all types (such as metals, semiconductors, polymer,

composite), the ability to control where in the material and at what rate energy is deposited, and the ability to modify surfaces over multiple length scales. Irradiation of the surface of a material with a short pulse laser has been shown to locally modify a range of possible properties such as surface morphology, hardness, wear and corrosion resistance of a material, while confining that modification to a very shallow penetration depth [4]. The confined microstructural and chemical modification allows the surface of the material to have different material and mechanical properties compared to the rest of the material. Applying laser surface treatment to multilayer thin films allows for local strengthening of the nanolaminate surface while retaining the ductility and toughness of the underlying multilayer structure.

2. Literature Review

2.1 Background of thin films and multilayers

Thin films are a subset of materials that have gained popularity in research and technology for their important role in a range of applications from microelectronics and photovoltaics [5, 6] to ultrahard tool and thermal barrier coatings [7]. The improved properties of thin films when compared to their bulk counterparts makes them very attractive when designing next generation material systems.

Multilayer thin films are material systems consisting of thin film layers of different materials deposited in a stack and encompasses simple systems of two films to many layers of varying thin films. When the multilayer is comprised of alternating layers with individual layer thickness less than 100 nm, the film may be classified as a nanolaminate. The flexibility in the material choice for individual layers makes multilayer thin films widely applicable to a variety of industries. The combination of materials used can give greater control and tunability of the

properties of the overall multilayer film. Nanolaminate materials have shown great promise for applications requiring high strength [8], wear resistance [9, 10], corrosion resistance [11], resistance to radiation damage [12, 13], specific optical or electromagnetic properties [14-16], and energy storage [17]. Structured multilayer polymeric films have been developed for targeted, time-released drug delivery in biomedical applications [18]. Metal/metal nitride multilayers are desirable for the ability to tailor the microstructure of the surface for bending and wear resistance, while designing the inner layers to optimize toughness [19]. The nanoscale thickness of the individual material layers combined with the interfacial structure of the multilayer often result in property improvements that surpass the expected result from a traditional rule of mixtures approach applicable in macroscale composite structures. Multilayer films can combine similar or dissimilar materials, including metal/metal, metal/ceramic, polymer/metal, and many other combinations.

2.2 Metallic multilayer strengthening mechanisms

Metallic multilayers are particularly desirable for their ultrahigh hardness and mechanical strength compared to bulk counterparts. The mechanical properties of metallic multilayers are not governed by the volume fraction of the constituent materials as typically governs bulk materials. Instead, the factors determining the material properties are dominated by the individual layer thickness and interface structure of the nanolaminate.

The effect of layer thickness on the strength of the multilayer has been explored for a variety of metallic nanolaminate combinations [2, 20-26]. The hardness of the various multilayers follow a similar trend as the individual layer thickness decreases, and the behavior can be described in three regions with different dominant dislocation mechanisms, as shown in Figure 1. When the individual layer thickness is relatively thick, on the order of 100 nm to the micron scale, dislocation

pile-up at the layer interface is the dominant deformation mechanism. The grain boundaries are the main mechanism to prevent dislocation propagation, and smaller grains increase the grain boundary concentration within the layer, so the strength is governed by the Hall-Petch relationship which relates strength to the grain size

$$\sigma_y = \sigma_0 + k\sqrt{d} \quad (1)$$

where σ_y is the yield strength, σ_0 is frictional stress required to move a dislocation, d is the layer thickness, and k is the Hall-Petch slope. As the individual layer thickness decreases to ~10 to ~100 nm, the dominant dislocation mechanism is confined layer slip as dislocation pile-up becomes limited by the layer thickness, and the hardness increases to its peak. As the layer thickness decreases to a few nm, the deformation mechanism changes from confined layer slip to interface crossing of a single dislocation and the strength is determined by the interface barrier strength and can result in softening of the multilayer [27-29]. Layer thickness has also been shown to affect material properties such as thermal stability [30], fracture behavior, and adhesion energy [31].

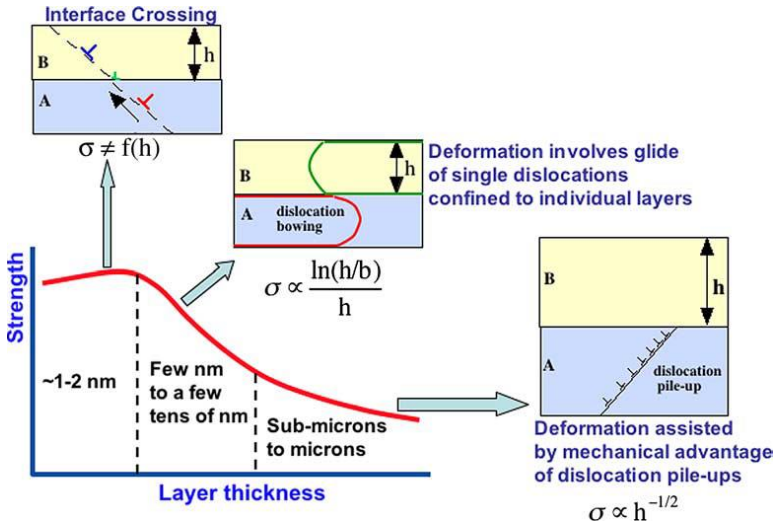

Figure 1. Schematic illustration of the dislocation mechanisms of multilayer strength at different length scales [27].

The interface structure between adjacent layers also contributes to the strength of the overall film. Interfaces serve as sources for nucleating dislocations, barriers impeding dislocation motions, and platforms for dislocation reactions. The strength of the interface is determined by the stress required to transmit dislocations across the interface, which is largely affected by the structure. Crystallographic structure, lattice parameters, and slip systems between the adjacent layers determine if the interface is coherent, semi-coherent, or incoherent. Coherent interfaces have similar crystallographic structures and similar lattice parameters in both layers, and the small lattice mismatch results in coherency stress which enhances the strength and hardness of the nanolaminate [29].

There are other factors which also influence strength of the nanolaminate, including grain morphology, the combination of the constituent phases, the presence of twins and nanostructuring, as well as interstitial additions such as fiber or nanoparticle reinforcement, solid solutions or intermetallic precipitates.

2.3 Material Systems of Interest

2.3.1 Ti/Ni

Ti/Ni multilayer thin films are of special interest as a material system due most commonly to its superior optical and mechanical properties. It has applications in soft X-ray and neutron optics, supermirrors, and high reflectance and polarization applications. Additionally, Ti/Ni has been used for controlled fabrication of Ti-Ni with improved control of the alloyed composition for uses as shape-memory alloys in MEMS and biocompatible devices. Ti/Ni has also been studied to investigate solid-state amorphization due to its large negative heat of mixing and the low temperature diffusion mobility of Ni, which makes amorphization energetically favorable [32].

Previous work [2] has examined the effects of the layer thickness and annealing temperature on the mechanical properties and microstructural evolution of Ti/Ni multilayer thin films. Layer thicknesses from 6 nm to 200 nm, and annealing temperatures from room temperature to 500°C were studied. The room temperature nanoindentation shows the expected strengthening trend for decreasing layer thickness as described above. As the annealing temperature increases, three trends emerge as shown in Figure 2:

(1) Thin individual layers of ≤ 16 nm monotonically increase in hardness as temperature increases.

(2) Intermediate layer thicknesses of 25 – 50 nm show an increase in hardness up to 300°C but decreasing with higher temperatures.

(3) Thick layers of ≥ 100 nm show no hardness change for low temperature annealing, increases in hardness up to 400°C, followed by a sharp decrease at 500°C.

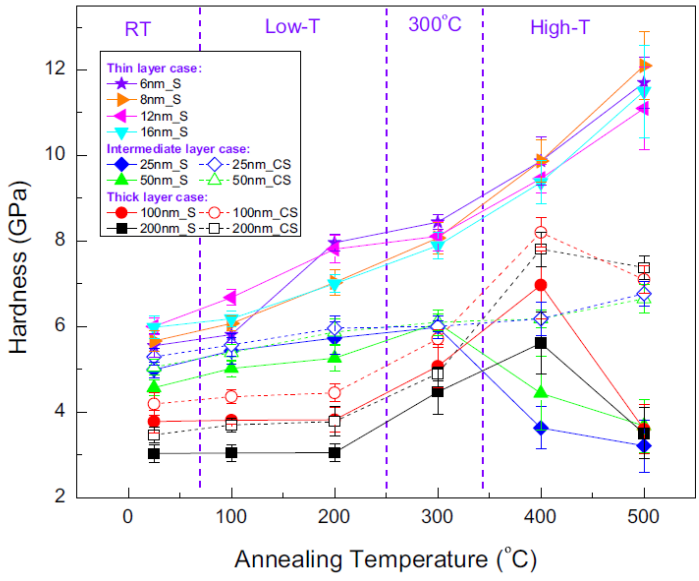

Figure 2. Indentation hardness of Ti/Ni multilayer films as a function of annealing temperature for different layer thickness [2].

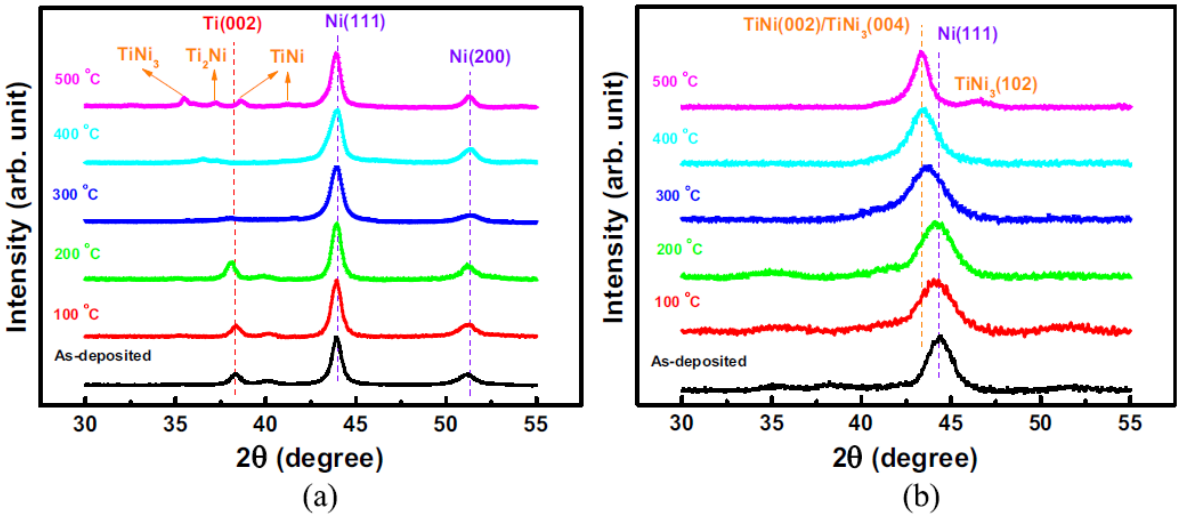

Figure 3. XRD spectra of as-deposited and annealed Ti/Ni multilayers with (a) 100 nm layer thickness, (b) 8 nm layer thickness [2].

Depending on the layer thickness, a different set of strengthening mechanisms applies to account for the observed hardness trends. For low temperature annealing, grain boundary relaxation is the main mechanism for improved hardness, with some evidence of diffusion. The thin layer samples are more susceptible to diffusion due to the high concentration of interfaces, leading to the more dramatic hardness increase compared to thicker layer films. As annealing temperature increases, there is sufficient energy to initiate grain boundary relaxation for the previously unaffected thick-layer films, while the thin-layer films experience more complete diffusion, solid solution strengthening, and intermetallic precipitation. High temperature annealing results in recrystallization and grain growth that supersedes the strengthening due to alloying and intermetallic formation at the interfaces, as shown in Figure 3, leading to softening of the thicker layers, while the thin layers were completely intermixed and continued to increase in hardness.

2.3.2 Cu/Al

Cu/Al is another example of a nanolaminate structure that demonstrates a significant increase in the hardness of the multilayer material compared to the monolithic films of its components. Early studies on the mechanics of Cu/Al confirmed enhanced properties, including hardness and fracture stress, as individual layer thicknesses of the Cu/Al films decrease [26]. Figure 4 shows the observed increase in hardness as the thickness decreases as compared to the hardness of Cu or Al films alone. The hardness continues to drastically increase as the thickness reduces to a few nanometers, which follows the typical strengthening mechanism of metallic multilayers previously discussed in Chapter 2.2.

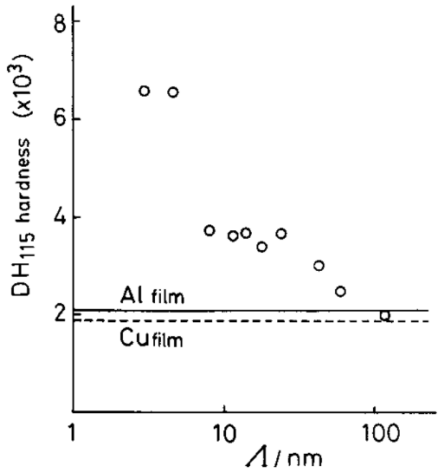

Figure 4. Microhardness of Cu/Al films vs bilayer period [26].

This increase in hardness due to layer thickness can be supplemented with annealing to promote intermixing at the film interfaces. From previous work [33], the hardness of Cu/Ni and Cu/Al thin films of various layer thicknesses were measured as a function of annealing temperature. In both material systems, an increase in the hardness was observed after annealing, however the extent of the improvement was dramatically different. The Cu/Ni films resulted in a moderate

increase of ~30%, while the Cu/Al films drastically increased in hardness by ~150% between annealing temperatures of 125 - 200°C, as shown in Figure 5.

This extreme discrepancy between the two materials is due to the formation of intermetallic particles in Cu/Al at the layer interfaces while the Cu/Ni interface is a simply intermixed solid solution. XRD analysis of the Cu/Al and Cu/Ni thin films as well as co-sputtered films of comparable thickness are shown in Figure 6. Cu/Al films show the generation of intermetallic phases after annealing at 150°C, and as annealing temperature continues to increase, so does the prevalence of intermetallic phases, corresponding with the drastic increase observed in the hardness. In contrast, Cu/Ni does not generate any intermetallic phases, consistent with the phase diagram associated with Cu and Ni alloys.

For both Cu/Al and Cu/Ni, the cosputtered film had superior hardness compared to the multilayered films. Cu-Ni cosputtered film had improved hardness but followed the same general trend as its multilayer counterpart. In contrast, the hardness of Cu-Al is nearly 11 GPa for both as-deposited and annealed conditions regardless of temperature, while the as-deposited multilayer only showed initial hardness values around 4 GPa. Here again, intermetallic precipitation is the main driver of the discrepancy. Cu-Ni does not have any possible intermetallic phases, so the grain boundary relaxation is the main strengthening mechanism in that case. The intermetallic phases present in Cu-Al under all temperature conditions indicate intermetallic formation is the strengthening mechanism.

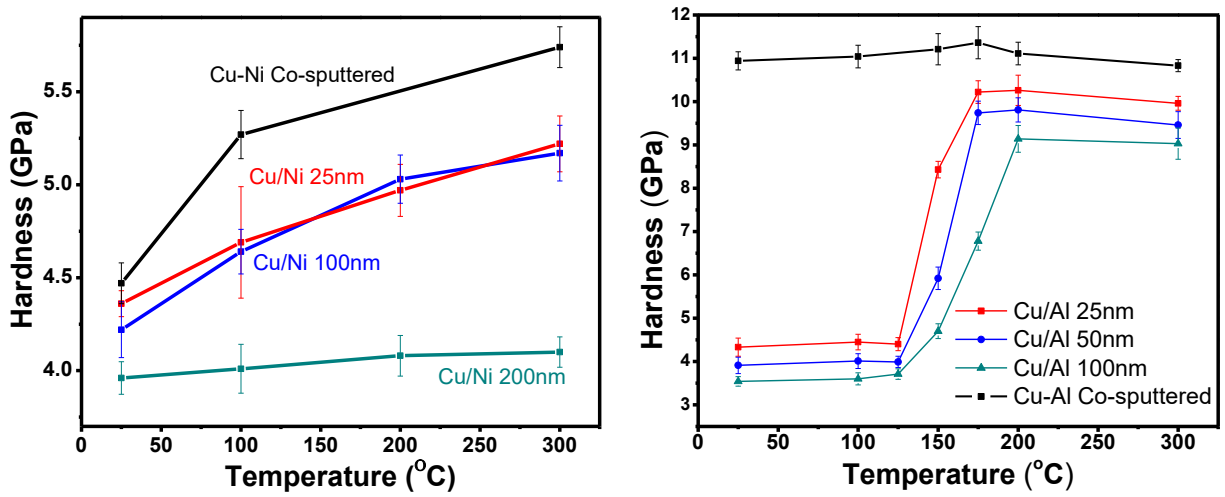

(a) (b)

Figure 5. Hardness of as-deposited and annealed (a) Cu/Ni and (b) Cu/Al with varying layer thickness [33]

A similar study [34] on a Cu/Al multilayer with an Al-rich environment (Cu layer thickness = 20 nm, Al layer thickness = 40 nm) showed similar strengthening. Grain boundary mediated diffusion promotes the formation of CuAl solid solution. Due to the low solubility of Cu into Al compared to the solubility of Al into Cu (0.15 at% vs 18 at% at 723 K), the solid solution in the Al side of the interface saturates first and promotes Al_2Cu precipitation. As annealing temperature increases, more complex intermetallic phases emerge, grow, and extend perpendicular and parallel to the interface. The intermetallic extending parallel along the interface operates as an intermediate layer creating a Cu/alloy/Al system, effectively reducing the length between adjacent layers. Figure 7 shows the progression of the three strengthening mechanisms dominating the hardness: interface alloying, reduced layer thickness, and grain size effect.

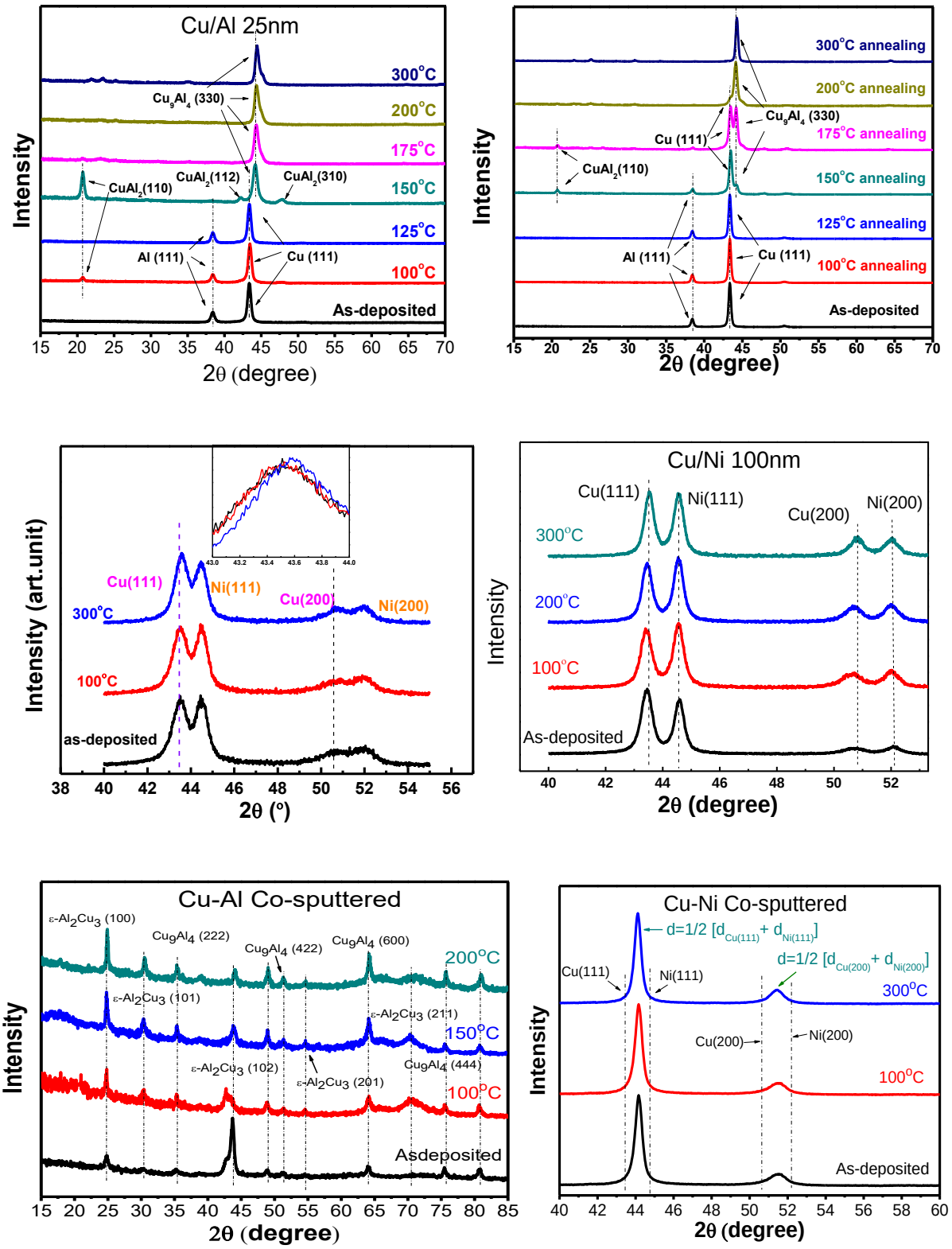

Figure 6. XRD spectra of as-deposited and annealed (a) Cu/Al 25 nm, (b) Cu/Al 100 nm, (c) Cu/Ni 25 nm, (d) Cu/Ni 100 nm, (e) co-sputtered Cu-Al, and (f) co-sputtered Cu-Ni [33].

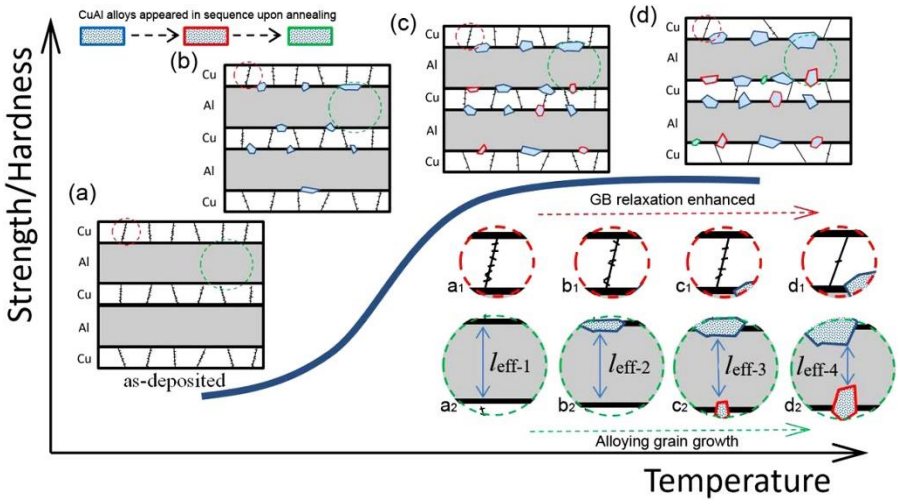

Figure 7. Schematic illustration of the strengthening mechanism of Cu/Al multilayers annealed at different temperature from 100 °C to 500 °C [34].

2.4 Laser ablation in material processing

Laser-based material processing has been used in a variety of applications due to the ability to achieve a desired response by precisely delivering large amounts of energy into confined regions of a material. Use cases span fabrication techniques like pulsed laser deposition and selective laser melting [35], machining processes like laser cutting, drilling, micro- and nanomachining [36], and laser processing from micro- and nanostructured solids like laser patterning [37], laser interference metallurgy [38, 39], and laser surface treatment[40-47] . Other applications included confined laser ablation [48], acoustic cleaning [49], and laser structuring though shock-wave induced delamination which is particularly useful for films on flexible or temperature-limited substrates [50]. In this work, the focus is laser surface treatment, which utilizes direct ablation or sub-ablation irradiation of the film to alter the material and mechanical characteristics of the surface.

Laser surface treatment has previously been studied in bulk materials, including metals [45, 51], ceramics [52], dielectrics [42], and composites [43, 53], to achieve improved mechanical properties such as hardness, fatigue, wear and corrosion resistance. Laser-induced period surface

structures (LIPSS) have been extensively reported and have been studied for their range of potential uses including micromachining of micro-electromechanical systems (MEMS), improved biointegration of biomaterials, and wetting behavior control. The study of LIPSS formation has been extended to thin film systems as well [36, 41, 46, 47]. The modification of surface characteristics like microstructure, surface roughness, and porosity are further supplemented by changes in the phase composition and chemical state such as oxidation, alloying, and intermetallic formation, all of which are confined to very shallow depths.

For metallic multilayer thin films, studies of laser treatment effects are split into two main focus areas: localized alloying and phase modification of the film layers [38-40, 46], and nanostructuring using selective ablation to control removal at specific depths through the film thickness [54, 55]. Farid et al. demonstrated the selective removal of the surface layer from a Mo/Al/Mo thin film stack using low fluence, single-pulse femtosecond treatment, and noted the challenge of ablating a high melting temperature material from a comparably low melting temperature material without damage to the underlying film [55]. A similar single-pulse study of the partial ablation of Ti/Al multilayers examined the fluence effect on the ablation behavior and remaining film structure [54]. In contrast, studies focused on intermixing and phase modification alter the properties of the multilayer without material removal. Ti/Al films treated using laser interference metallurgy have demonstrated the development of localized Ti-Al intermixed regions extending through the film thickness, effectively resulting in a multiscale composite structure, with nanoscale alternating layers through the film thickness, and alternating multilayer and intermixed regions along the length of the film, as shown in Figure 8 [39].

The surface intermixing of Al/Ti films has also been demonstrated after laser treatment with both picosecond [40, 56] and nanosecond [56] pulse lasers. The resulting films show the

development of an intermixed region supplanting the layered structure at the film surface, with the thickness of the intermixed region dependent on the treatment energy and the pulse duration of the laser.

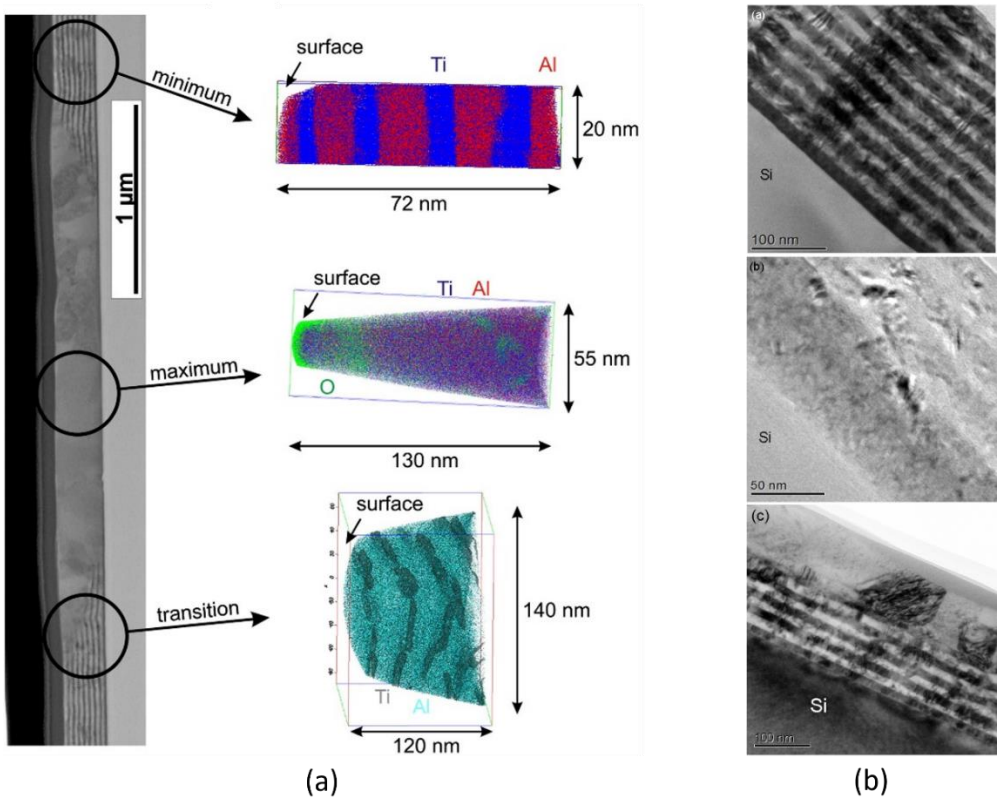

Figure 8. Al/Ti multilayer intermixing zones via laser interference metallurgy [39], Al/Ti multilayer as-deposited, fully intermixed after nanosecond laser treatment, and partially intermixed after picosecond laser treatment [56].

The effectiveness of surface modification by laser irradiation can change based on a variety of factors, including incident energy and the interaction time scale. The incident energy is not the output energy of the laser pulse, but the portion of that energy that is absorbed or transmitted into the material. Reflectivity and optical absorption determine the penetration depth of the laser treatment and are dependent on the laser wavelength and the optical properties of the material. The interaction time scale refers to the relative difference in laser-induced electron excitation rate and the thermalization time for the excited electrons to transfer energy to the lattice [57].

Thermalization time for most metals is on the order of 10^{-12} – 10^{-10} s. For short pulse nanosecond lasers, the laser-excitation rate is low compared to the thermalization rate, and the absorbed laser energy is considered directly transformed to heat. For ultra-short femtosecond pulse lasers, the excitation rate is high, leading to high energy build-up in the electrons and results in a non-thermal modification, though high repetition rates can result in thermal effects. Picosecond lasers generally result in a combination of thermal and non-thermal effects.

3. Research Objectives

The goal of this work is to control the strengthening of metallic multilayer films through the application of laser surface treatment. As-deposited metallic multilayers have demonstrated superior hardness compared to monolithic films of the component materials. Annealing of metallic multilayers, particularly for both Ti/Ni and Cu/Al, has been shown to further increase strength, resulting in ultrahard/ultra-strength materials. Current studies of laser surface treatment on multilayer films have shown the potential for localized surface modification and intermixing, but focus on the microstructural change, not the mechanical properties. This work examined the mechanical properties in conjunction with the microstructural change and demonstrated the applicability of laser surface treatment as a targeted strengthening technique.

To accomplish this, there are several factors that must be considered for their effects on the microstructural evolution and surface strengthening of laser-treated films.

Objective 1: Effect of laser pulse energy: investigate the effect of varying laser pulse energy on the microstructure and surface strengthening.

Objective 2: Effect of layer thickness and film thickness: study the effect of both the individual layer thickness and the total film thickness on the interface intermixing and mechanical properties after laser surface treatment.

Objective 3: Intermetallic precipitation: investigate the extent of the intermetallic precipitation due to laser surface treatment and its effect on the final microstructure and mechanical properties on an intermetallic rich system such as Cu/Al.

Objective 4: Approximate manufacturing conditions: develop a scale-up approach for large area surface treatment.

4. Experimental Methods

4.1 Magnetron Sputtering

Thin films can be deposited through a variety of methods, generally classified between chemical and physical deposition methods. Magnetron sputtering is a physical vapor deposition process that is very commonly used to create thin films and multilayer materials due to the ability to deposit crystalline and amorphous films with high film thickness uniformity. Inert argon gas is ionized by an applied electric field to create plasma consisting of Ar ions and electrons. A magnetic field near the target attracts the electrons and confines the plasma near the target. The energized Ar ions are accelerated towards the negatively charged target and impinge on the surface of a target of the desired material to be deposited, ejecting atoms of the target material which are deposited on the substrate.

Multilayer materials in this study were fabricated using an ultra-high vacuum magnetron sputtering system (Orion-5-UHV, AJA International). This system has three target guns, one RF and two DC, which allows the deposition of up to three materials without removing the substrate

from the chamber. The base vacuum of the chamber is 10^{-8} mbar, and during depositions the argon gas pressure was ~4 mTorr. The films were deposited on single crystal Si wafers. The details of the deposition for the Ti/Ni and the Cu/Al material systems are discussed below.

Ti/Ni multilayer thin films were deposited on single crystal Si (100) wafers using Ti (99.995%) and Ni (99.999%) targets in the DC guns. Alternating layers were deposited on the Si substrate with Ti as the first layer and Ni as the final layer. The deposition power was 100 W, and the sputtering time of each layer was controlled to maintain the desired layer thickness. The sputtering rates for Ti and Ni were 2.44 and 3.37 nm/min, respectively. In each sample, the Ti layer has the same thickness as the Ni layer. In this work, two options for individual layer thickness were deposited, 20 nm and 50 nm, as well as two options for the total thickness of the multilayer films, 500 nm and 1 μm. This resulted in four layer-thickness/film-thickness combinations: 20 nm/500 nm, 50 nm/500 nm, 20 nm/1 μm, 50 nm/1 μm.

Cu/Al multilayer thin films were deposited on single crystal Si wafers using Cu (99.995%) and Al (99.999%) targets in the DC guns. Alternating layers were deposited on the Si substrate with Al as the first and last layer due to the superior adhesion of Al and Si as well as the slightly improved absorption of Al at 1064 nm when compared to Cu. A Ti capping layer was added to the surface to further improve absorption of the laser, which is discussed in Chapter 5.2.1.1. All individual layers were 25 nm, for a total Cu/Al thickness of either 500 nm or 1 μm, and a total film thickness overall of 550 nm or 1.05 μm accounting for the additional Al adhesion layer and Ti capping layer. Films were deposited at 100 W with an Ar gas pressure of 4 mTorr, and sputter time was controlled to achieve 25 nm individual layer thicknesses. The sputtering rates of Al, Cu, and Ti were 5.4, 11.3, and 0.22 nm/min, respectively.

4.2 Laser Surface Treatment

The sputtered multilayer samples were subsequently irradiated by a pulsed 1064 nm laser to modify the surface chemical and physical properties of the multilayer film. Laser surface treatment refers to the direct irradiation of the film surface. In this work, two different pulsed 1064 nm lasers were used, requiring slightly different corresponding setups shown in Figure 9 and Figure 10. The energy per pulse was measured by a high energy pyroelectric sensor (PE25BF-DIF-C, Ophir Photonics) that is rated for an energy range from 100 μJ – 10 J. The multilayer sample was mounted on a manual rotation stage to set the angle of incidence between the incoming laser light and the surface normal of the multilayer. Using an oblique angle of incidence was required due to the high reflectivity of the samples as well as avoiding spallation of the film due to reflection of the induced compressive stress. The rotation stage was mounted to a two-axis translation stage to precisely control the position of the laser spot on the sample surface.

The Ti/Ni multilayers were treated with a picosecond pulse laser (Leopard SS-2, Continuum), which has pulse duration of 120 ps, repetition rate of 5 Hz, and maximum energy per pulse of 260 mJ. The corresponding experimental setup is shown in Figure 9. The output pulse energy for this laser is fixed at 260 mJ, so a half-wave plate and polarizer were used as an optical attenuator to vary and control the pulse energy. The attenuation is adjusted according to the following relationship:

$$\begin{cases} E_1 = E_0 \\ \gamma = \beta \end{cases} \tag{2}$$

$$E_2 = E_1 \cos(\beta + \gamma + \alpha) = E_0 \cos(2\beta + \alpha) \tag{3}$$

where E_0, E_1, and E_2 are the magnitudes of the light vector at the output of the laser, after the half-wave plate, and after the polarizer, respectively, β and γ are the entrance and exit angles of the

incident laser beam with respect to the fast axis of the half-wave plate, and α is the angle between the native polarization direction of the laser and the fixed polarization direction of the polarizer. Rotating the half-wave plate changes β, and varies the portion of the laser that is aligned with the polarizer, thus varying the deposited pulse energy. The laser was then focused through a plano-convex lens, and by varying the distance between the sample surface and the lens up to the lens's focal distance, the diameter of the irradiated area of the sample surface, or spot size, can be adjusted from the original beam diameter of 10 mm to 3 mm. The angle of incidence was fixed at 67.5° due to the reflectivity of the film. All samples were irradiated with 50 pulses. The spot size was held constant at 3 mm diameter, as measured for a 0° incidence angle at full energy. The energy per pulse varied between 25 mJ – 150 mJ. To determine the effect of pulse energy on the surface modification and strengthening of Ti/Ni, layer thickness and total film thickness were set to 20 nm/500 nm respectively. To incorporate the effect of layer thickness, 50 nm/500 nm films were introduced, followed by 20 nm/1 μm and 50 nm/1 μm films to investigate the effect of varying the total film thickness.

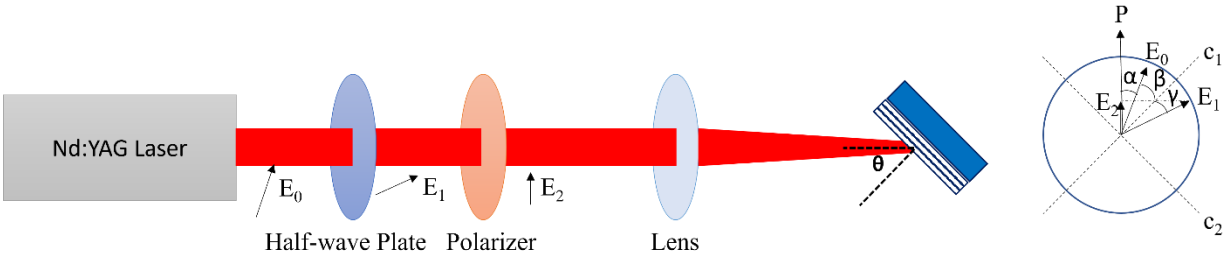

Figure 9. Experimental setup for picosecond pulse laser treatment used for processing the Ti/Ni and Cu/Al multilayer films.

The Cu/Al multilayers were treated with the picosecond pulse laser described above as well as a nanosecond pulse laser (Tempest 300 10 Hz, New Wave), which has a pulse duration of 5 ns, a variable repetition rate up to 10 Hz, and maximum energy per pulse of 275 mJ. The

corresponding experimental setup is shown in Figure 10. The output pulse energy for this laser is controlled by Q-switching, which allows the output energy to be controlled by changing the delay in the fire signal using a pulse delay generator (Model 9514, Quantum Composers). The repetition rate used in this testing was 5 Hz. The spot size of the beam was reduced from the 7 mm beam diameter to a 3.5 mm spot diameter by mechanical filtering with an iris shutter sized to 3.5 mm due to a local inhomogeneity in the laser beam profile. A detailed exploratory study of applying different optical solutions to address the inhomogeneity is discussed in the Appendix. The angle of incidence was initially set to 45°, but 30°, 55°, and 67° were also used during this study. Energy per pulse varied from 25 mJ – 100 mJ, and number of pulses varied from 1 – 250 pulses.

Figure 10. Experimental setup for the nanosecond pulse laser treatment used for processing the Cu/Al multilayer films controlling spot size using mechanical filtering by selectively blocking portions of the beam with an iris aperture.

The difference in pulse duration between the nanosecond laser and the picosecond laser changes the laser-material interaction as well as the peak power of the laser pulse during the laser treatment even when all other parameters are kept constant. The peak power for a laser with a Gaussian distribution can be approximated as

$$P_{peak} \approx 0.94 \frac{E_L}{\tau_L} \tag{4}$$

where E_L is laser pulse energy and τ_L is the laser pulse duration [58]. For the same pulse energy, this results in a peak power for the picosecond laser that is 41.7 times the peak power of the

nanosecond laser. The pulse duration, along with thermal diffusivity, D, also determines the thermal diffusion length, l_T, defining the heat affected zone of the laser processing as

$$l_T = 2\sqrt{D\tau_L} \tag{5}$$

$$D = \frac{\kappa_t}{\rho c_p} \tag{6}$$

where κ_t is thermal conductivity, ρ is density, and c_p is specific heat of the material [56, 58]. Calculating l_T using an average of D_{Cu} and D_{Al}, the thermal diffusion lengths for treatment with the nanosecond and picosecond lasers are approximately 1460 nm and 226 nm respectively.

4.3 Analysis

4.3.1 Microstructure Characterization

Several techniques were used to characterize the multilayer films in both as-deposited and post-laser treatment conditions. Scanning electron microscopy (SEM) was used to observe the evolution of the surface and cross-sectional morphologies of the as-deposited and laser-treated multilayer films. In this work, SEM was done using the FEI SEM XL30 and Apreo S Variable Pressure SEM (ThermoFisher Scientific) available in UW Molecular Analysis Facility. X-ray diffraction (XRD) was used to examine the crystalline structure of the multilayer films and to determine the intermetallic precipitation within the multilayer structure. XRD of the Ti/Ni films was performed with a step of 0.06 °/s to study the crystallinity of the treated and non-treated films with enough detail to capture changes in phase composition. Cu/Al films were scanned with an 11° increment. The Si peak associated with the substrate was masked out of the data for clarity.

4.3.2 Nanoindentation

Nanoindentation is a common technique to measure the mechanical properties of thin films, most commonly hardness and elastic modulus. An indenter tip with a known geometry penetrates the material and is withdrawn according to a set loading, holding, and unloading function leaving an indent on the sample surface. As the load is applied, the surface undergoes both elastic and plastic deformation, and as the load is removed only the elastic deformation is recovered. A schematic of the deformation behavior is shown in Figure 11(a). A load-displacement curve as shown in Figure 11(b) is generated for the full loading cycle, and by analyzing the unloading curve, the hardness and elastic modulus of the film can be calculated [59]. Nanoindentation hardness is defined as

$$H = \frac{P_{max}}{A_c} \tag{7}$$

where H is the material hardness, P_{max} is the maximum load, and A_c is the contact area projected based on contact depth h_c and the shape of the indenter tip. The reduced modulus E_r, or the modulus of the indenter-material system, can be determined based on the initial slope of the unloading curve S and A_c according to the equation

$$E_r = \frac{\sqrt{\pi}}{2\sqrt{A_c}} S \tag{8}$$

Often, the reduced modulus value is the modulus reported in literature, but it is possible to isolate the elastic modulus of the film using the relationship

$$\frac{1}{E_r} = \frac{(1-\nu_m{}^2)}{E_m} + \frac{(1-\nu_i{}^2)}{E_i} \tag{9}$$

where E_m and ν_m are the elastic modulus and Poisson's ratio of the sample and E_i and ν_i are properties for the indenter tip. For a diamond tip, the elastic modulus is 1140 GPa and Poisson's ratio is 0.07.

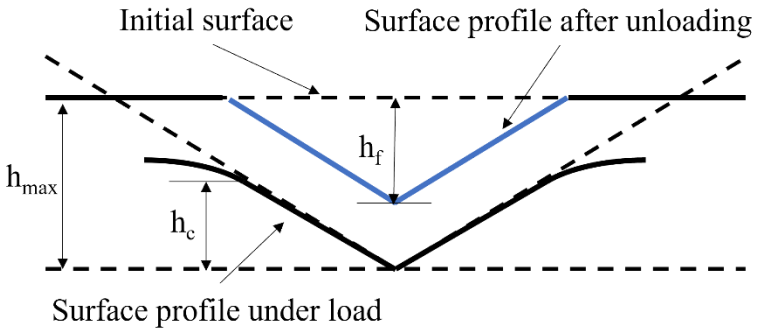

(a)

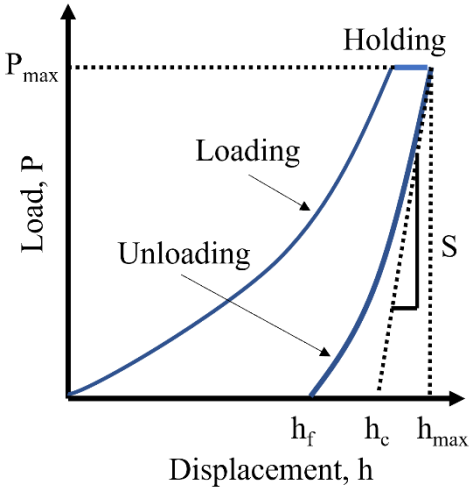

(b)

Figure 11. (a) Schematic of deformation behavior before and after indentation, (b) typical nanoindentation load-displacement curve.

In this study, the nanoindentation was completed using a Hysitron Ubi-1 Nanoindenter and a Hysitron TI 980 TriboIndenter with a Berkovich tip which has a three-sided pyramid geometry. For each indent, a trapezoidal load function was used with a 10 s loading, a 5 s hold at the peak load, and a 10 s unloading. An array of indents was completed on each sample to obtain the

average hardness and observe any trends in the hardness with respect to the depth of the indent, particularly in the shallow indents where the effect of laser surface treatment is more prevalent. For surfaces too rough for nanoindentation after laser treatment with high pulse energy, manual polishing was performed using 0.3 μm alumina slurry for 30 seconds to remove a few nanometers of rough material.

5. Results and Discussion

5.1 Ti/Ni

As discussed in Chapter 2.3.1, annealing of Ti/Ni multilayers resulted in strengthening of the material, though the extent depended both on the layer thickness and the annealing temperature. In the annealed conditions, several strengthening mechanisms compete for dominance, leading to different trends in hardness as temperature increased. This makes Ti/Ni an interesting material to study the effect of laser surface treatment for targeted strengthening. The following sections describe the effects of laser energy, layer thickness, and film thickness on laser-induced microstructural evolution and surface strengthening in Ti/Ni multilayers, the results of which have been previously published [60, 61] and readapted for this study.

5.1.1 Objective 1: Laser energy effect

To study laser energy effect, the Ti/Ni samples had an individual layer thickness of 20 nm and a total film thickness of 500 nm. The samples were treated using the picosecond laser setup described in Figure 9. The samples were treated with 50 successive pulses with a repetition rate of 5 Hz. Other details of the laser testing were described in Chapter 4.2. The energy per pulse varied from 50 mJ to 150 mJ.

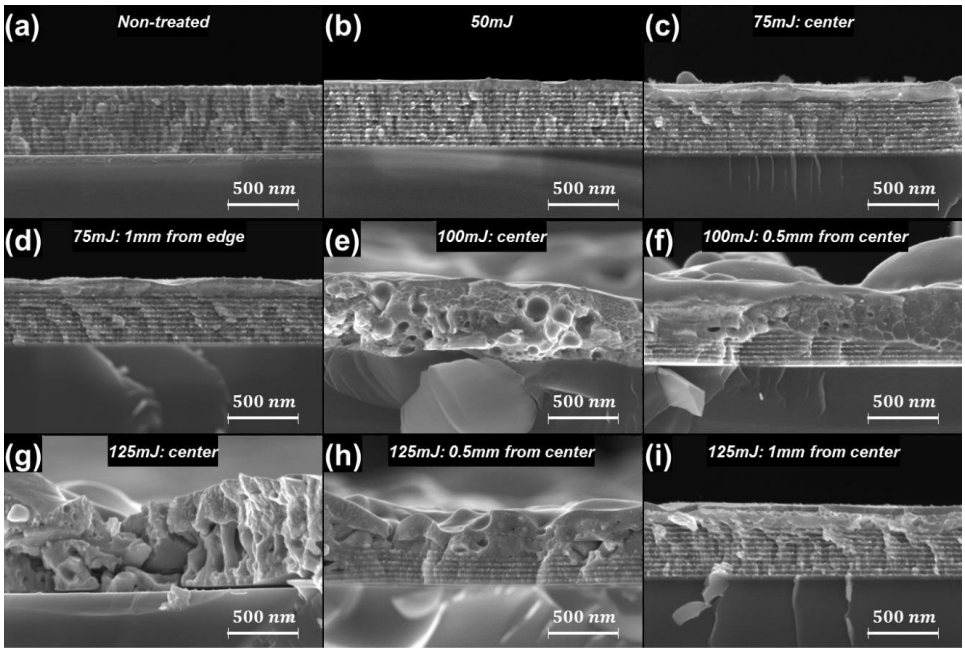

Figure 12. SEM images of cross-sectional morphologies for: (a) as-deposited, and (b-i) laser-treated Ti/Ni by different pulse energies from 50 - 125 mJ.

Cross-sectional SEM of the microstructural evolution with increasing pulse energies is shown in Figure 12. The as-deposited cross-section shows the well-defined alternating layer structure with Ti shown as the dark layers and Ni as the light. After laser treatment with 50 successive pulses at 50 mJ, a thin intermixed layer is formed with a thickness of ~50 nm. The remaining layers show no significant change. Increasing the pulse energy to 75 mJ, shown in Figure 12(c – d), results in an increase in the intermixed layer thickness to ~100 nm. The 100 mJ laser treatment resulted in a nonuniform response depending on the position within the irradiated area. Figure 12(e) shows a fully intermixed film in the center of the irradiated area, but as distance from the center increases, there is decreasing intermixed layer thickness. This behavior continues as pulse energy increases to 125 mJ. The spatial dependence of intermixed layer thickness is attributed to the Gaussian distribution of the laser beam profile.

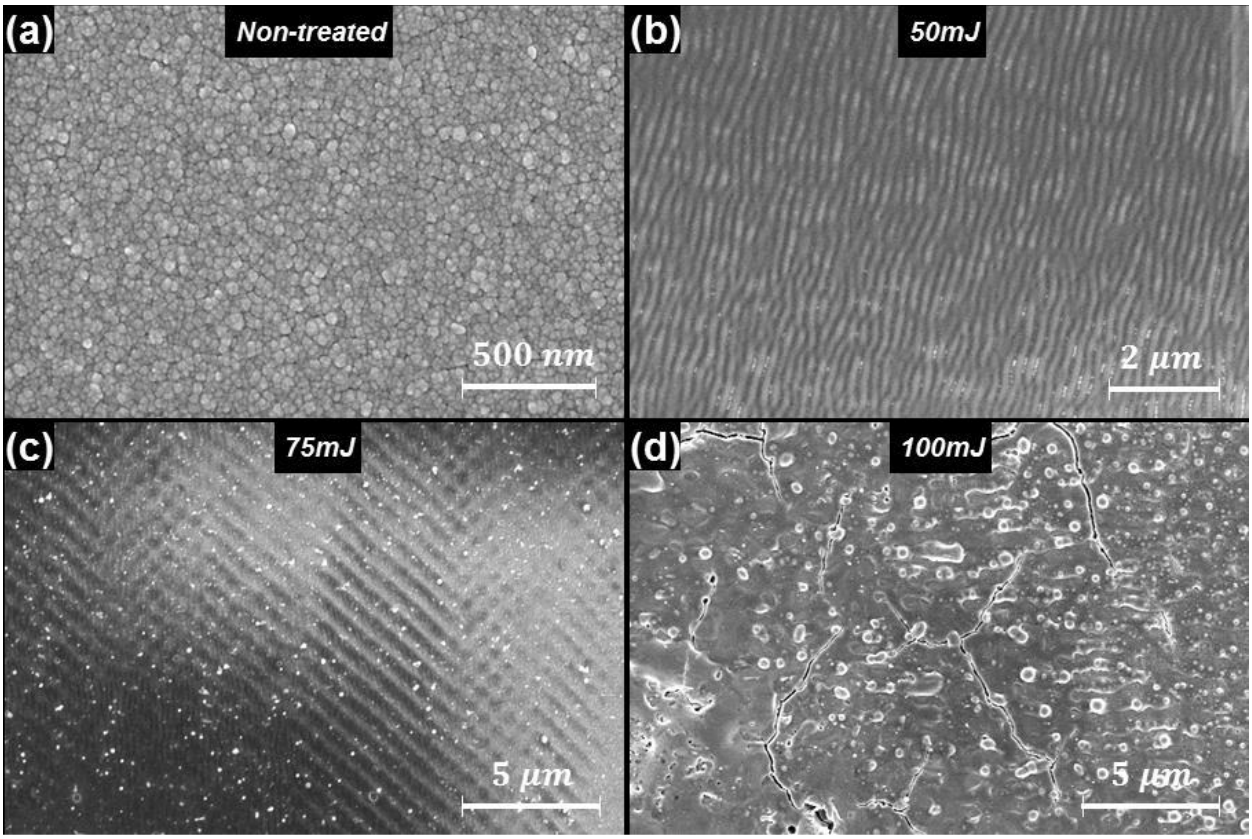

Figure 13. SEM of surface morphologies for as-deposited and laser-treated Ti/Ni from 50 - 100 mJ.

The surface morphology of Ti/Ni after laser-treatment at various energies is shown in Figure 13. The as-deposited surface is smooth, with clear uniform grain structure. After 50 mJ laser treatment, the relatively smooth surface is maintained and vertical ripples form on the surface. After 75 mJ, the ripple structure has been replaced by a cross-hatched structure. These ripple and cross-hatch structures may be attributed to interference between the incident beam and scattered beam parallel to the substrate, which is the dominant theory for LIPSS formation. For high energy treatment of 100 mJ, the resulting surface is melted with high roughness, bubbles, voids, and cracks.

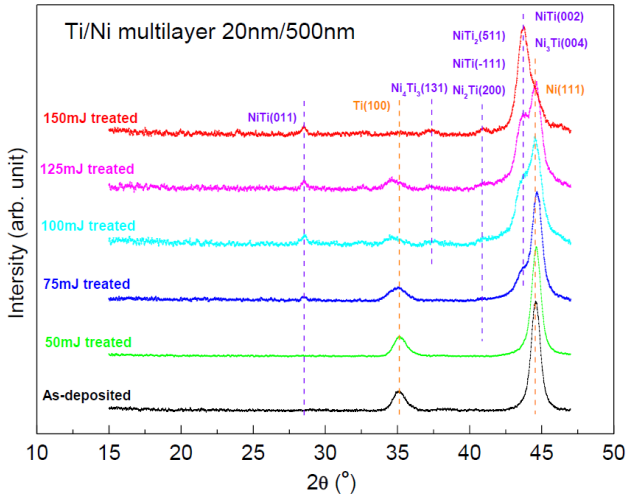

Figure 14. XRD spectra for as-deposited and laser-treated Ti/Ni multilayers for pulse energies from 50 - 150 mJ.

Figure 14 shows the XRD spectra for as-deposited and laser-treated samples for pulse energies from 50 – 150 mJ. The as-deposited case shows two distinct peaks corresponding to Ti (100) and Ni (111). The 50 mJ case shows no change in the spectra, indicating that the intermixed layer does not include Ti-Ni intermetallic formation. At 75 mJ, new intermetallic peaks start to appear, which continue to grow in intensity as pulse energy increases, indicating that higher pulse energy promotes intermetallic formation. As energy increases, there is also the generation of more intermetallic phases. After treatment with 150 mJ, the original Ti (100) and Ni (111) peaks have disappeared, and only intermetallic peaks are detected.

Nanoindentation hardness results for as-deposited and laser-treated Ti/Ni are shown in Figure 15. The as-deposited results show a consistent hardness of ~5.6 GPa regardless of contact depth. Similar hardness values and distributions are observed for the 25 mJ and 50 mJ laser-treated films. As pulse energy increases to 75 mJ and higher, there is significant scattering of the hardness values due to the increased roughness of the surface. Nanoindentation is optimized for smooth surfaces, as supported by the tight distribution for the as-deposited and low energy samples with

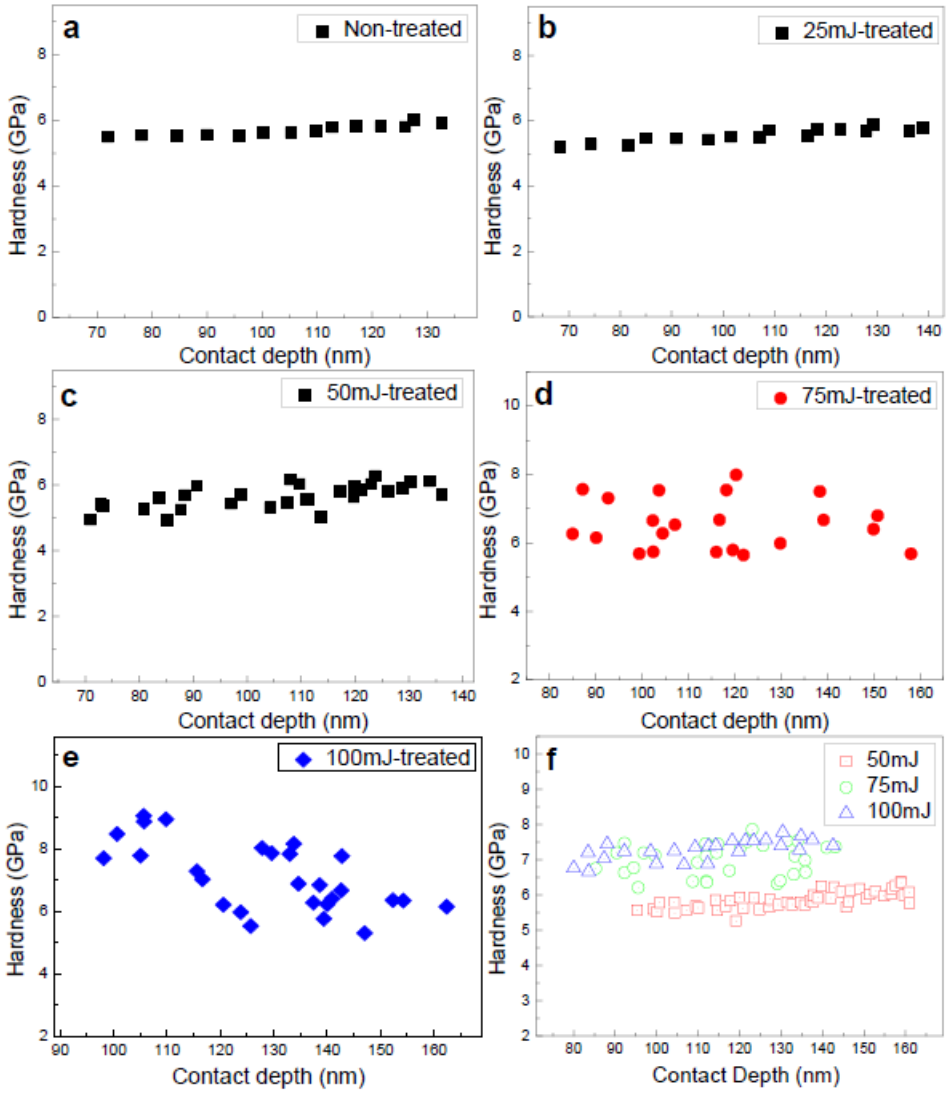

Figure 15. Hardness distribution with contact depth for (a) as-deposited and (b-e) laser-treated Ti/Ni with varying pulse energy from 25 - 100 mJ, (f) for polished laser-treated samples from 50 - 100 mJ.

high surface quality. To reduce the effect of surface roughness, mechanical polishing was done as described in Chapter 4.3.2. Figure 15(f) shows the hardness distribution of the polished 50, 75, and 100 mJ samples. The 50 mJ sample shows similar behavior to the unpolished result, but the polished 75 and 100 mJ samples show improved consistency in the hardness distribution. Interestingly, the improved hardness distribution for the polished sample treated with 75 mJ shows

no change in hardness with the indentation depth up to 160 nm, but the thickness of the intermixed layer was only ~100 nm. This indicates that the multilayers near the surface intermixed layer may be strengthened, even as they maintain their structure.

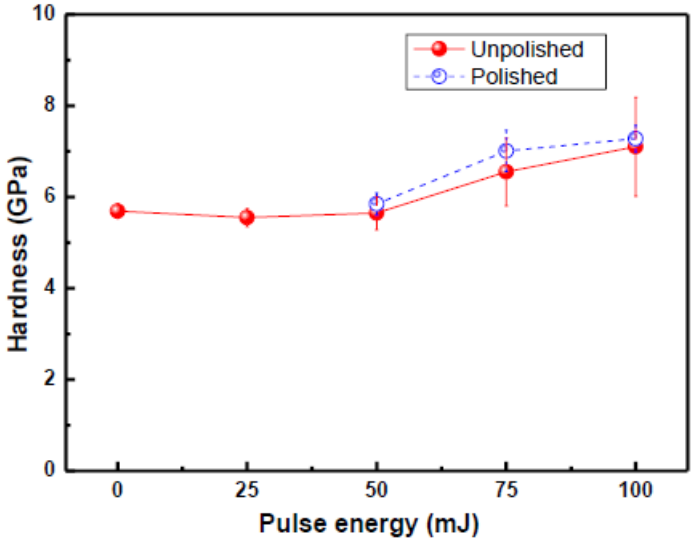

Figure 16. Average hardness as a function of laser pulse energy for unpolished and polished Ti/Ni films.

The average hardness of as-deposited and laser-treated Ti/Ni films, as well as polished results as they are applicable, are shown in Figure 16. Low pulse energy treatments, including 25 and 50 mJ, show no significant change in hardness. There is a 50 nm intermixed layer formed after laser treatment at 50 mJ, however this indicates that the intermixed layer has similar hardness to the multilayer or is too thin to contribute to the overall hardness. High energy treatment shows an increase in the average hardness after 75 mJ, that continues to increase with increasing energy. This corresponds with the XRD evidence of the onset of intermetallic formation at 75 mJ. With increasing energy, intermetallic formation increased, and a subsequent increase in hardness is observed.

5.1.2 Objective 2: Layer and film thickness effects

To investigate the effect of individual layer thickness, the previous results for 20 nm/500 nm Ti/Ni films were compared to a set of 50 nm/500 nm films. To investigate film thickness, 20 nm/1 μm and 50 nm/1 μm Ti/Ni films were included. The same laser treatment conditions were applied.

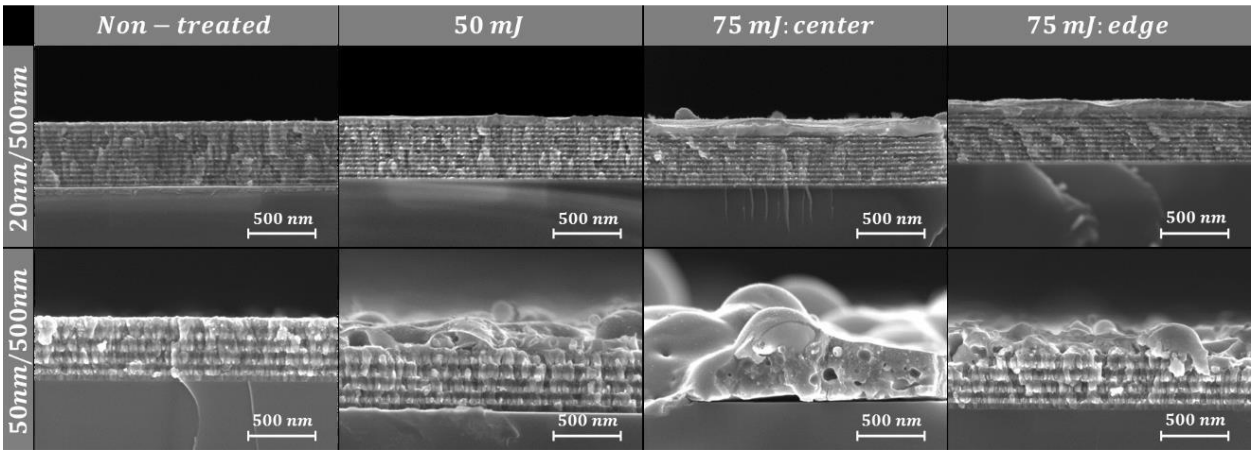

Figure 17. Cross-sectional SEM of as-deposited and laser-treated 500 nm Ti/Ni films with 20 nm (top row) and 50 nm (bottom row) layer thickness.

SEM of the cross-section for 500 nm Ti/Ni films with layer thickness of 20 and 50 nm are shown in Figure 17. After treatment with 50 mJ, the 20 nm case shows the development of an ~50 nm, smooth intermixed layer, while comparable conditions in the 50 nm case result in an ~100 nm, rough intermixed layer. Treatment at 75 mJ results in an increase in thickness to ~100 nm for the 20 nm case, maintaining relative smoothness of the intermixed layer, and shows a uniform layer thickness with respect to location within the irradiate area. Alternatively, the 50 nm case results in a fully intermixed film in the center, with partial intermixing near the edge of the irradiated area. The 20 nm case also showed this nonuniform behavior at higher pulse energies, as shown in Figure 12.

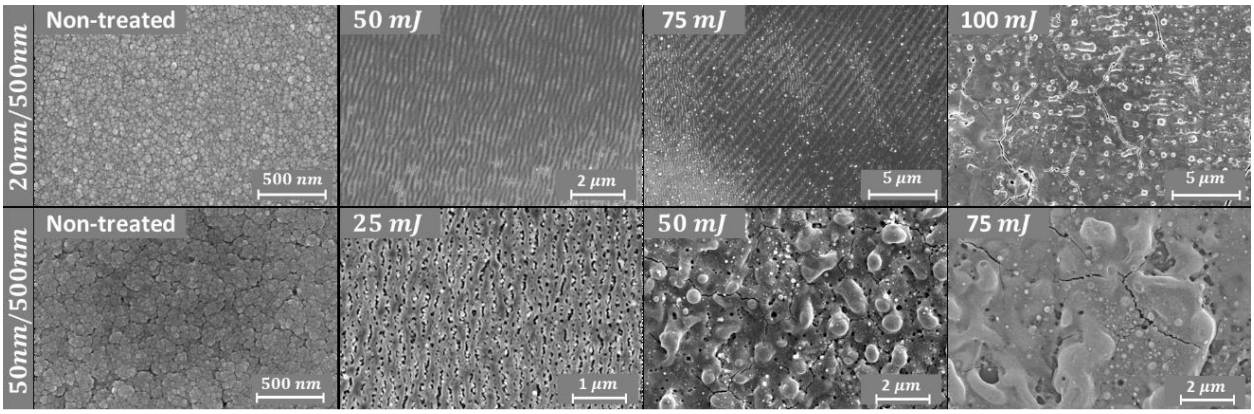

Figure 18. Surface SEM of as-deposited and laser-treated 500 nm Ti/Ni films with 20 nm (top row) and 50 nm (bottom row) layer thickness.

The corresponding surface morphologies for the 20 nm and 50 nm cases are shown in Figure 18. The as-deposited samples show similar smooth surfaces with uniform grain distribution. The 20 nm case developed shallow ripple and cross-hatched textures while remaining relatively smooth after laser treatment with 50 and 75 mJ, respectively. Higher energy testing resulted in a rough melted surface. The 50 nm case shows no evidence of the smooth ripple behaviors, even at a lower treatment energy of 25 mJ. Instead, at 25 mJ a melted vertical ripple structure is observed, likely caused by a combination of LIPSS superimposed on a lightly melted surface. Increasing the pulse energy to ≥ 50 mJ results in rough melted surfaces.

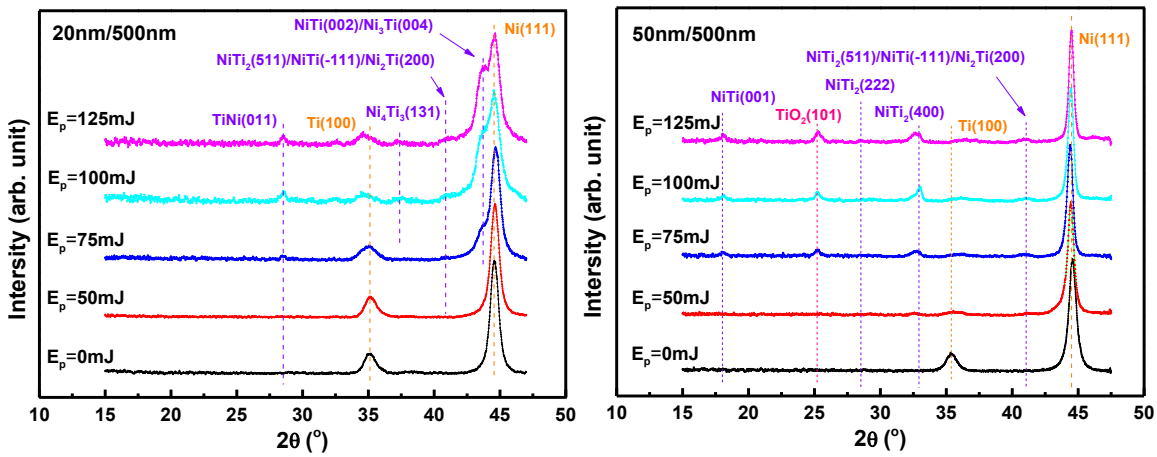

Figure 19. XRD spectra of as-deposited and laser-treated 500 nm Ti/Ni films with (left) 20 nm and (right) 50 nm layer thickness.

The evolution of the phase composition corresponding to the observed surface and cross-sectional morphology changes were studied using XRD. Figure 19 shows the XRD patterns of the as-deposited and laser-treated films for the 20 nm and 50 nm layer thickness cases. As previously described, the 20 nm case shows the onset of intermetallic phases after laser treatments at 75 mJ, and increasing intermetallic formation in terms of peak strength and formation of new peaks as pulse energy continues to increase. Figure 19(b) shows the microstructure evolution for the 50 nm case. After 50 mJ, the baseline Ti peak observed in the as-deposited sample has nearly disappeared and a very small $NiTi_2$ (400) peak has started to form. As pulse energy increases, the small $NiTi_2$ peak becomes more intense, and other intermetallic phases begin to precipitate. Additionally, the 50 nm case shows the formation of a TiO_2 peak after 75 mJ treatment that intensifies with higher energy testing.

The intermetallic formation in both layer thickness cases follows a similar trend: an intermetallic phase forms initially after a critical energy, that phase intensifies with an increase in treatment energy, then additional intermetallic phases form. However, the specific Ti-Ni intermetallic phases initially formed are different depending on the layer thickness. In the 20 nm case, the initial intermetallic phase that precipitates is NiTi, while in the 50 nm case the initial phase is $NiTi_2$. When the individual layer is thick, the diffused Ni could be surrounded in a Ti-rich environment, leading to intermetallic phases with higher Ti fraction.

Figure 21(a-b) shows the hardness as a function of pulse energy for the 20 nm/500 nm and 50 nm/500 nm Ti/Ni thin films. The as-deposited Ti/Ni films have hardness values of 5.8 GPa for the 20 nm case and 5.4 GPa for the 50 nm case. The 20 nm case shows no change in hardness after 50 mJ laser treatment, but shows a significant increase as pulse energy increases, which is consistent in both the unpolished and polished samples. The roughness of the surfaces in the 50

nm case necessitated polishing in order to have reliable nanoindentation results. The polished samples show an increase in hardness for treatment energies greater than 25 mJ, but the increase is less significant. After treatment with 100 mJ, the hardness in the 20 nm case increased to nearly 7.3 GPa, an ~25% increase, compared to the ~5% increase observed for the 50 nm case.

Extending the study to include total film thickness, Figure 20 shows the cross-section and surface morphologies of 50 and 75 mJ treatment for 500 nm and 1 μm Ti/Ni films with individual layer thicknesses of 20 nm and 50 nm. The 1 μm films show the formation of a thin, smooth intermixed layer with uniform distribution, regardless of layer thickness, compared to the drastic difference between the intermixed layer development observed for the two 500 nm films. Comparing the cross-sectional morphologies of all four cases indicates less energy may be

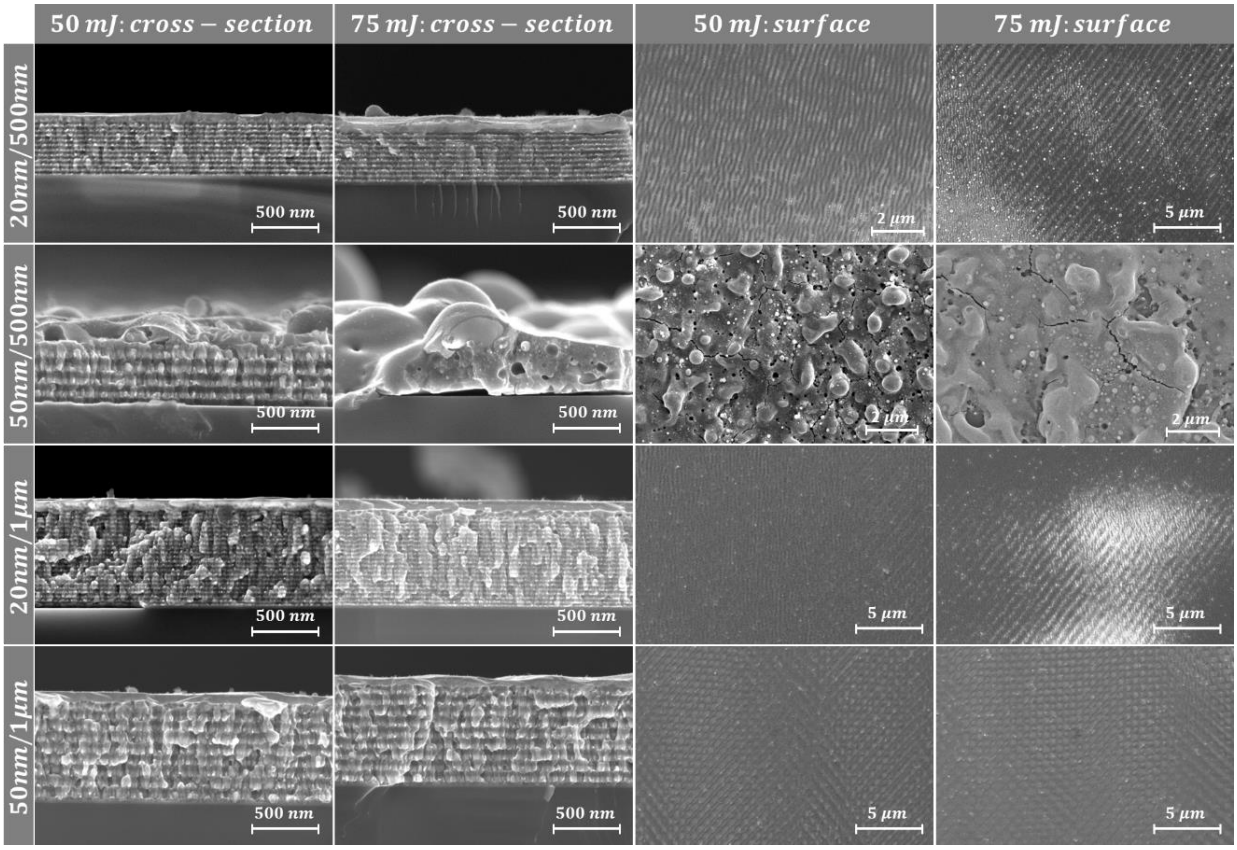

Figure 20. Cross-section and surface morphologies for laser-treated 500 nm and 1 μm Ti/Ni films with 20 nm and 50 nm layer thickness.

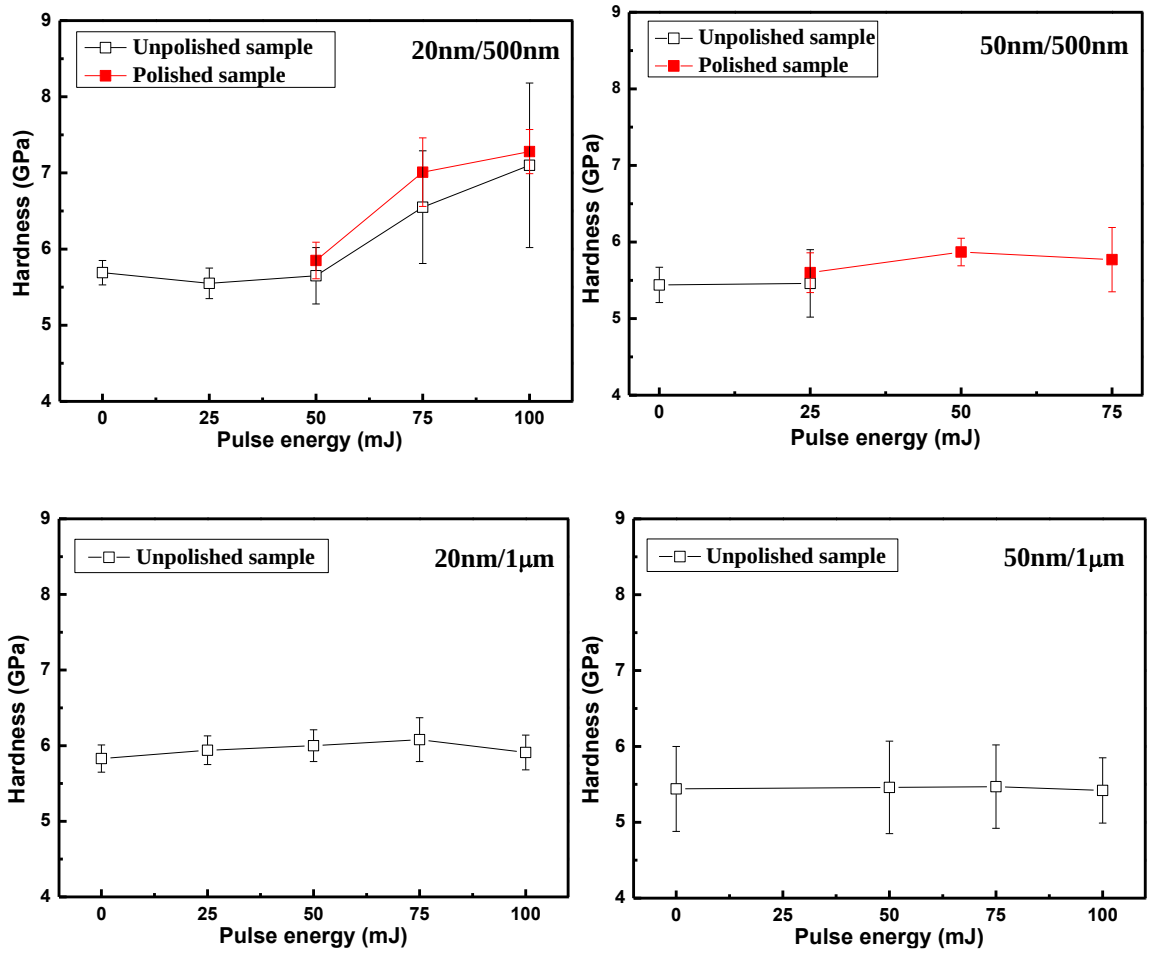

Figure 21. Hardness as a function of pulse energy of as-deposited and laser-treated Ti/Ni films with layer thickness/total film thickness combinations of: (a) 20 nm/500 nm, (b) 50 nm/500 nm, (c) 20 nm/1 μm, (d) 50 nm/1 μm.

dissipated from the surface as the ratio of layer thickness to film thickness increases. The surface morphology evolution supports this as the highest ratio, 50 nm/500 nm, shows a rough melted surface of bubbles, voids, and cracks, while the 20 nm/500 nm and the two 1 μm films show similar ripples and cross-hatched morphologies. The periodic surface structures in the 1 μm films were observed for pulse energies up to 125 mJ. XRD spectra of the laser-treated 1 μm Ti/Ni films showed no obvious change from the as-deposited results, indicating the accumulated energy to form the intermixed layer is not sufficient to generate intermetallic phases for the range of laser conditions tested in this study. This is supported by the nanoindentation results presented in Figure

21, showing that as pulse energy increases, the 1 μm thick films (Figure 21(c – d)) have no significant increase in hardness regardless of pulse energy or layer thickness, as compared to the 20nm/500 nm film (Figure 21(a)) which shows hardness increases corresponding the intermetallic precipitation within the intermixed layer.

5.2 Cu/Al

The potential of Cu/Al for ultrahard surface development was inspired by the drastic increase in hardness for annealed Cu/Al as described in Chapter 2.3.2. Additionally, the Ti/Ni results described above show the development of an intermixed layer and an increase in hardness associated with intermetallic formation induced by laser surface treatment. The following sections describe the results of laser-induced surface strengthening through intermetallic precipitation in Cu/Al multilayers using lasers with different pulse durations, altering testing parameters to optimize for intermetallic phase generation, and applying array laser surface treatment to investigate the applicability in an industrial context.

5.2.1 Objective 3: Intermetallic precipitation for surface strengthening

5.2.1.1 Considerations for Cu/Al laser treatment: reflectivity and thermal conductivity

Initial design of the laser treatment experiment for the Cu/Al films combined the material structure previously used in the studies of annealing effects discussed in Chapter 2.3.2, and the laser treatment conditions applied in the Ti/Ni laser testing: 25 nm layers of Cu and Al for a total film thickness of 1 μm, laser tested with 50 pulses at various energies. However, the results revealed unique challenges for laser treating Cu/Al that had not been present in the laser treatment of Ti/Ni: high reflectivity and thermal conductivity. Initial testing was completed with the nanosecond laser (5 ns pulse duration), but the effect of high reflectivity is present with both the nanosecond and picosecond laser systems.

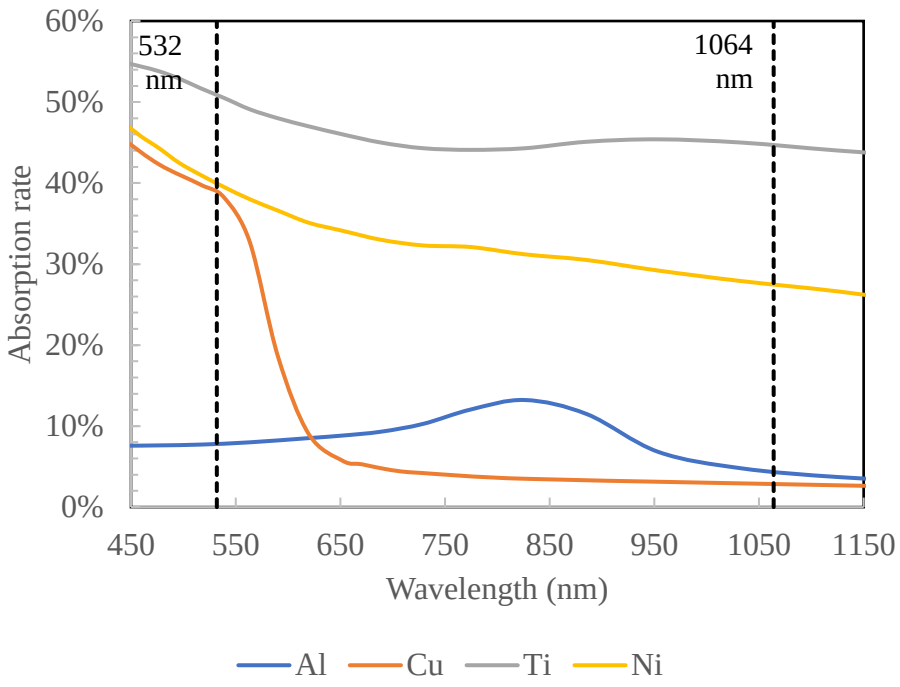

Figure 22. Absorption rate with respect to wavelength for Cu, Al, Ti, and Ni. Adapted from [62].

Figure 22 shows the absorption rate of the key component materials in this study, Cu and Al, as well as Ti and Ni for comparison. For laser treatment using 1064 nm lasers, the absorption rate of Al is ~5% and Cu is ~3%, compared to the rates for Ti and Ni which are ~45% and ~27% respectively. For the Cu/Al multilayer, more than 90% of the incident energy is reflected from the surface, vastly reducing the efficiency and efficacy of laser treatment. Due to this high reflectivity, the angle of incidence for laser surface treatment of the Cu/Al multilayer was reduced from 67° to 45° to increase absorption while still operating at an oblique angle to avoid spallation of the film. Additionally, the observed material response shown in Figure 23 delineates a sharp transition between the onset of surface modification and spalled film removal. Evidence of surface morphology modification is shown in the 50 mJ treatment case, but only for an ~500 μm diameter zone of the total 4 mm irradiated area. Nanoindentation of the modified region (Figure 24) showed a dramatic increase in hardness from the as-deposited value of 4.8 GPa to 8.6 GPa, but only for

the dark zones on the surface, which account for a negligible fraction of the total surface area. An increase in treatment energy of only 5 mJ results in complete ablation of the film.

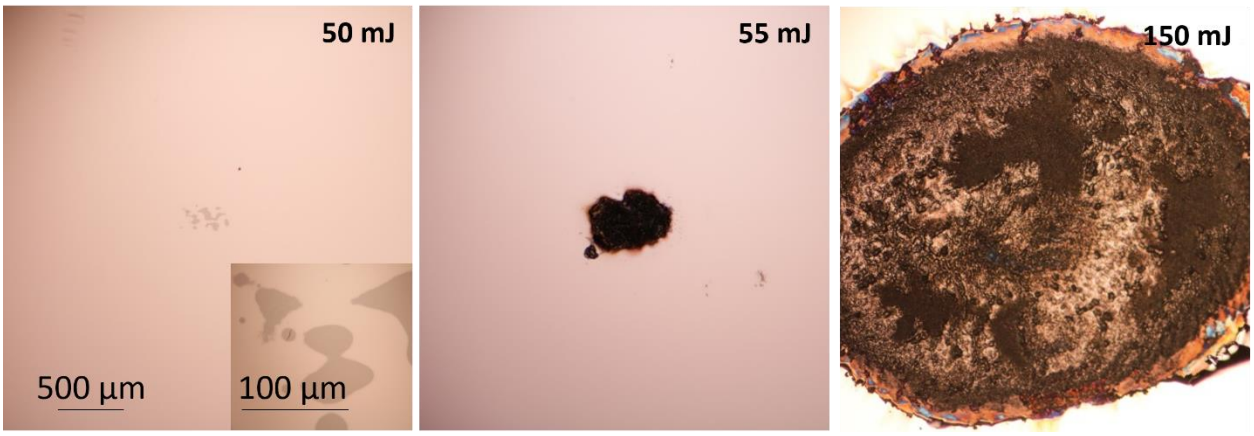

Figure 23. Optical microscopy of Cu/Al 25 nm/1 µm film treated with increasing energy. Evidence of morphological change is present at 50 mJ (magnified in the inset), followed by spall for the same treatment at 55 mJ, both of which are observed only in a small portion of the total irradiated area, as indicated by high energy treatment.

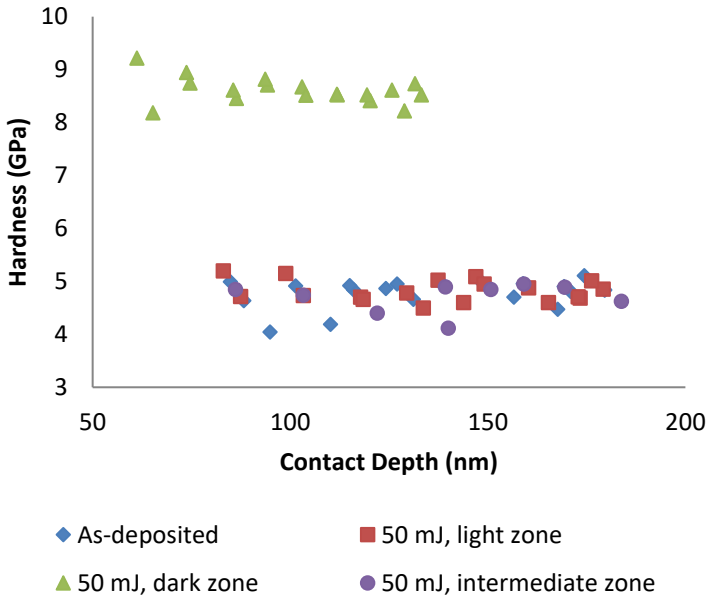

Figure 24. Hardness of as-deposited and 50 mJ laser-treated Cu/Al across different surface regions. Intermediate zone is the light areas that occur between two dark zones.

To improve the absorption of the laser energy, a 25 nm Ti layer was added to the surface as an energy absorbing layer. The addition of the Ti layer has two potential benefits: the increased absorption of the incident laser energy and minimizing the topographical change at the film surface

due to the high melting temperature of Ti. With the inclusion of the Ti absorbing layer, the surface morphology after laser treatment showed significant changes. Figure 25 shows two representative samples of the change in surface morphology after laser treatment with and without the Ti layer.

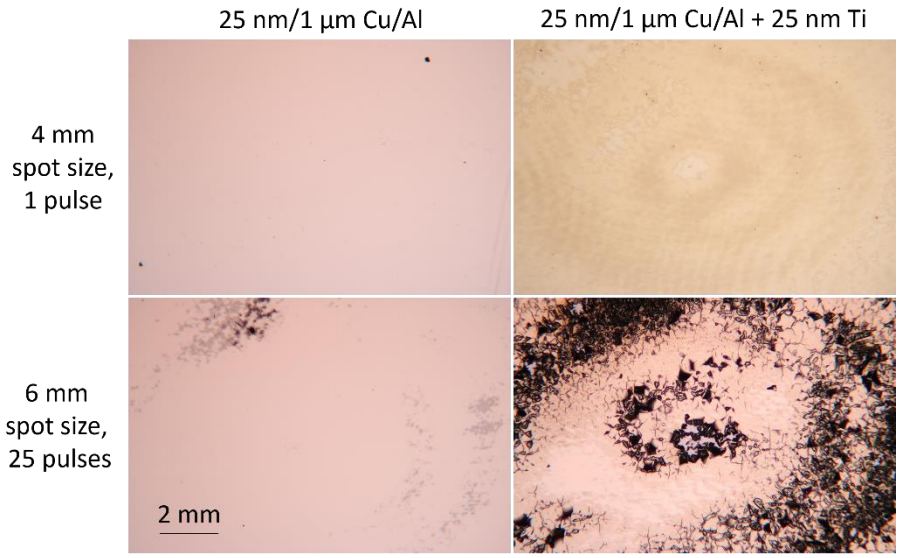

Figure 25. Representative surfaces samples treated with constant fluence 0.47 J/cm^2 after laser treatment with and without the Ti absorbing layer.

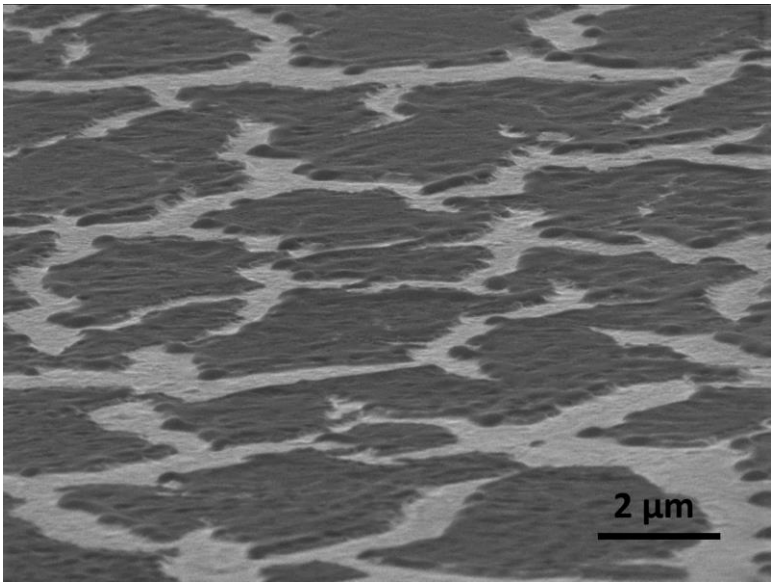

Figure 26. Microcracking of the Ti absorbing layer after laser-treatment.

An unexpected effect of including a Ti absorbing layer is the formation of microcracking on the film surface in areas of the spot exposed to irradiation. The microcracks begin to form after as few as 1 pulse and continue to widen with increasing pulse number. An example of the microcracks is shown Figure 26. Visually, the cracks seem to be limited to the Ti surface film, however SPM line scans across the cracks completed using the nanoindenter show an average depth of 58 nm after treatment with 25 pulses, which increases to an average depth of 99 nm after 50 pulses. The deposited Ti film was only 25 nm, indicating the cracks do eventually penetrate into the multilayer structure. While this microcracking is undesirable, the cracks do not appear to drive overall failure within the multilayer structure. This finding in conjunction with the obvious increase in pulse energy absorption made the inclusion of a Ti absorbing layer overall advantageous for the laser treatment process. All samples going forward incorporate the 25 nm Ti absorbing layer.

The microcracking is also indicative of the other consideration that arises as a consequence of changing the material system to Cu and Al, which is the significant difference in thermal properties from the Ti/Ni material system to the Cu/Al material system. Table 1 shows the thermal properties of the four component materials discussed in this study. Cu and Al have much higher thermal conductivity compared to Ti and Ni, which results in higher thermal diffusivity within the Cu/Al multilayer structure. As discussed in Chapter 4.2, the thermal diffusivity and pulse duration of the laser used determine the thermal penetration depth and the subsequent surface confinement of the treatment effects. Using an average thermal diffusivity based on the two materials in each material system, the laser penetration depth after picosecond laser treatment for Ti/Ni is approximately 90 nm compared to approximately 230 nm for Cu/Al. The nanosecond laser treatment of Cu/Al

resulted in a thermal penetration depth of approximately 1460 nm, which encompasses the entire thickness of the films. The impact of the Ti capping layer was not considered in these calculations.

Table 1. Thermal properties of Al, Cu, Ti, and Ni. Adapted from [62].

Material	Melting Temperature (°C)	Thermal conductivity (W/(m·K))	Thermal expansion coefficient (µm/(m·K))	Thermal diffusivity (mm^2/s)
Aluminum	660	237	23.1	97.9
Copper	1085	401	16.5	116
Titanium	1670	21.9	8.6	9.28
Nickel	1455	90.7	13.4	23.0

5.2.1.2 Effect of pulse duration

As a part of this study, two lasers were available to be used for treatment of the multilayer with different pulse durations: a nanosecond pulsed laser with a pulse duration of 5 ns, and a picosecond pulsed laser with a pulse duration of 120 ps. As described in Chapter 4.2, the difference in pulse duration leads to changes in thermal penetration depth, the peak power per pulse for a given pulse energy, and the mechanism of absorbed energy transfer into the material. This section discusses the observed differences in the results of nanosecond and picosecond laser surface treatment.

5.2.1.2.1 Nanosecond laser surface treatment (ns-LST)

Initial treatment of the 1 µm Cu/Al film with 25 nm Ti capping layer using the nanosecond pulse laser resulted in the development of a ringed surface pattern of alternating behavior corresponding to minima and maxima within the laser mode. In the minima, the surface retained the morphology, microstructure, and corresponding mechanical properties of the as-deposited film. In the maxima, there were observable increases in the hardness, but these rings also became the likely location for film failure with increasing energy or pulse number. Additionally, the upper left quadrant consistently showed early delamination due to an inhomogeneity in the beam profile that

was unique to this specific laser. Several techniques were attempted to improve the uniformity the resulting surface treatment while compensating for the inhomogeneous profile to prevent premature failure of the film, and the results are discussed in detail in the Appendix. Of the methods attempted, the most promising result was achieved with the addition of an iris aperture used to simultaneously control the spot size of the surface treatment and block the inhomogeneous portion of the laser profile. This mechanical filtering by physically blocking the undesirable portion of the beam used an iris with a 3.5 mm aperture to reduce the initial 7 mm diameter, 275 mJ energy pulse to a 3.5 mm spot size with 66 mJ of energy.

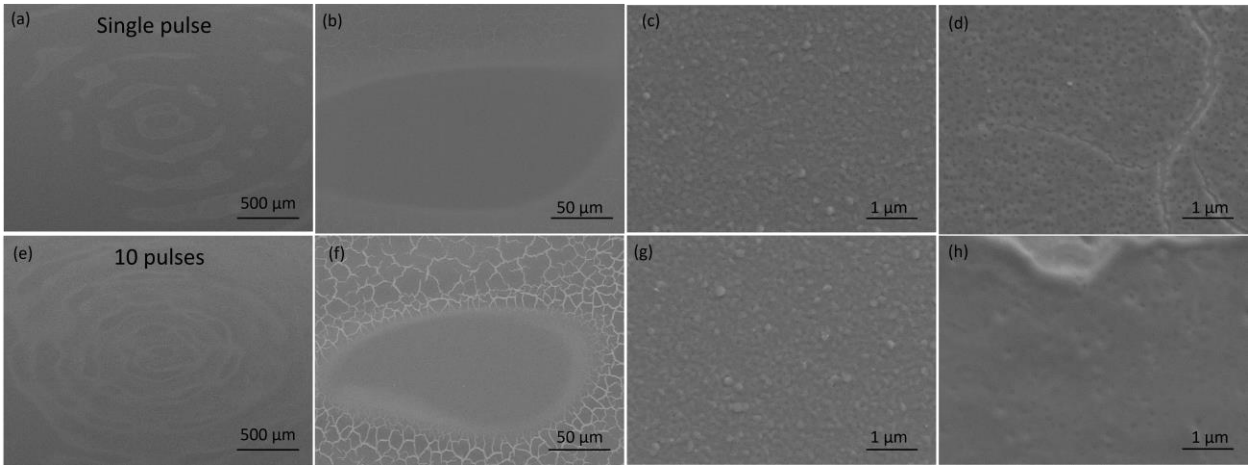

Figure 27. Surface evolution for iris-filtered laser treatment at 66 mJ for (a-d) 1 pulse, (e-h) 10 pulses. (b, f) show the center of the spot with an unaffected zone in the center (c, g), and a ring of affected material distinctly showing surface microcracking (d, h).

Figure 27 shows the resulting surface morphology evolution for the full 66 mJ laser treatment after a single pulse and 10 successive pulses. The alternating regions of affected and unaffected behavior are still present, which are clearly distinguishable by the microcracking of the Ti absorbing layer. As the exposure increases with increasing pulse number, the microcracking becomes more distinct. Interestingly, the ringed structure in this case is dominated by the diffraction minima and maxima caused by passing through the iris aperture and superimposed on the portion of the original rings caused by the laser mode. This introduced an interesting possibility

for improved uniformity by controlling the distance between the rings that is discussed in more detail in the Appendix. The minima regions for 1 and 10 pulse treatment, shown in Figure 27 (c) and (g), both show similar grain structure that compares with the as-deposited surface morphology, while the Ti absorbing layer shows a lightly melted surface covered in voids after a single pulse but further exposures results in a smooth, fully melted Ti island after 10 pulses.

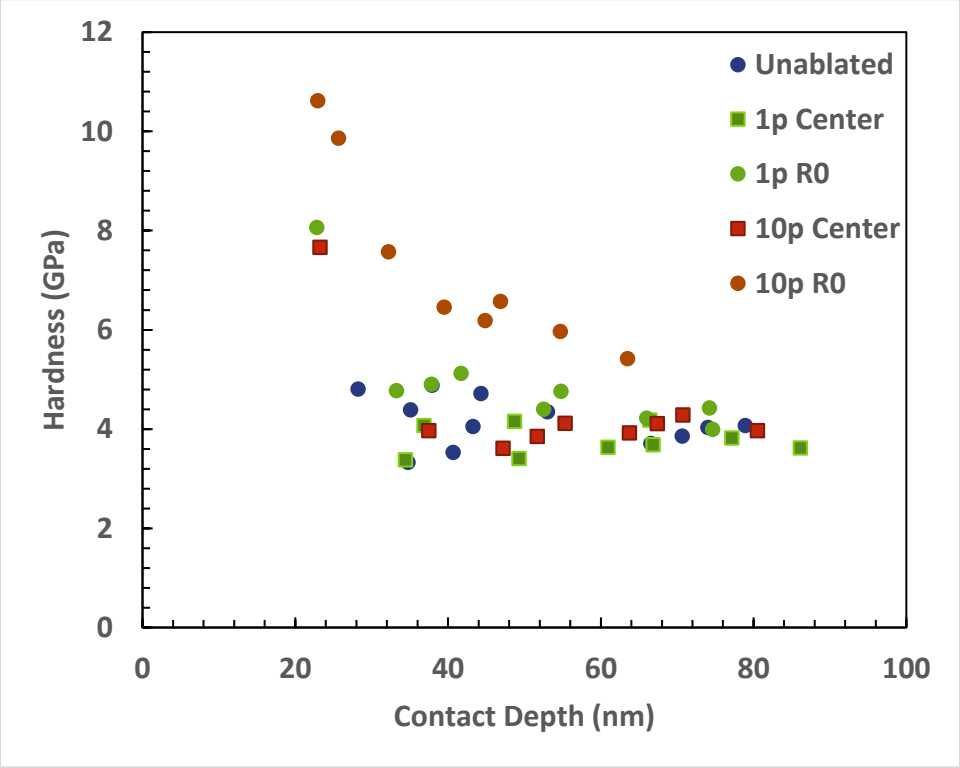

Figure 28. Hardness development in the center and R0 zones depicted in Figure 35.

Figure 28 shows the hardness developments in the unaffected center zones and the ring for the single pulse and 10 pulse cases. The center zones and the single pulse ring zone show good agreement with the as-deposited film results. However, the 10-pulse ring hardness shows drastic improvement at shallow indentation depths. The highest results occur for contact depths ~25 nm, which corresponds with the first interface between the Ti and Al surface layers. Although the individual layer structure is shown to be preserved through at least 25 pulses (Figure 29), even if full intermixing is not present, the interfaces between adjacent layers are the initialization point

for diffusion between layers. Figure 30(a) shows the full XRD spectra for the iris-filtered laser-treated Cu/Al. The stacked spectra do not indicate any significant change in the microstructure, however, by overlapping the spectra, a faint peak is revealed as shown in Figure 30(b). As pulse number increases, a small plateau on the back leg of the main Cu peak indicates the formation of a small quantity of Cu_9Al_4. The miniscule magnitude is likely due to the very localized formation due to the surface patterning as well as the shallow depth of precipitation compared to the total analyzed depth in XRD.

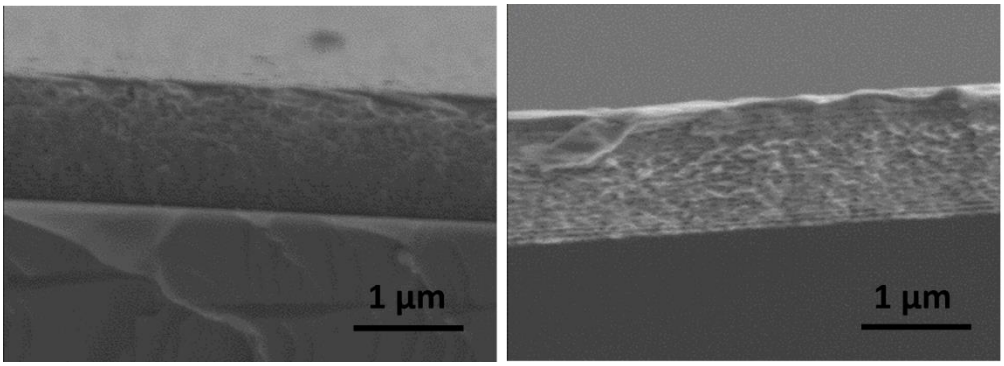

Figure 29. Cross-section of as-deposited and laser-treated Cu/Al after 25 pulses at 66 mJ for iris-filtered testing.

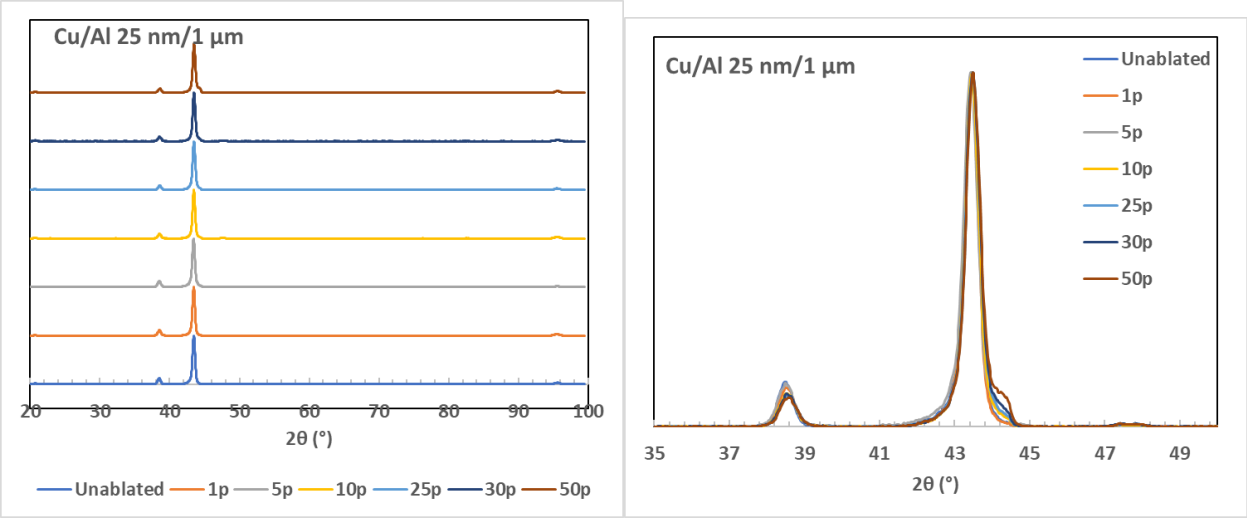

(a) (b)

Figure 30. XRD spectra laser-treated Cu/Al comparing (a) the entire spectra and (b) the small plateau forming at the base of the main Cu peak.

5.2.1.2.2 Picosecond laser surface treatment (ps-LST)

Due to lower thermal penetration depth when applying laser surface treatment with a shorter pulse duration, the picosecond laser is theoretically more desirable for improved surface confinement of microstructural changes in the multilayer structure. Additionally, in this case, ps-LST avoids the unique complications associated with the inhomogeneous beam profile present in the nanosecond laser. Rather than controlling spot size with mechanical filtering, the spot size was controlled with the standard method of focusing through a plano-convex lens and altering the distance between the lens and the sample surface. Using the ns-LST parameters as a comparison, ps-LST of a 1 μm Cu/Al multilayer with the Ti cap was tested with 66 mJ, 3.5 mm spot size, 45° angle of incidence, and a frequency of 5 Hz. Figure 31 shows the surface morphology after 5

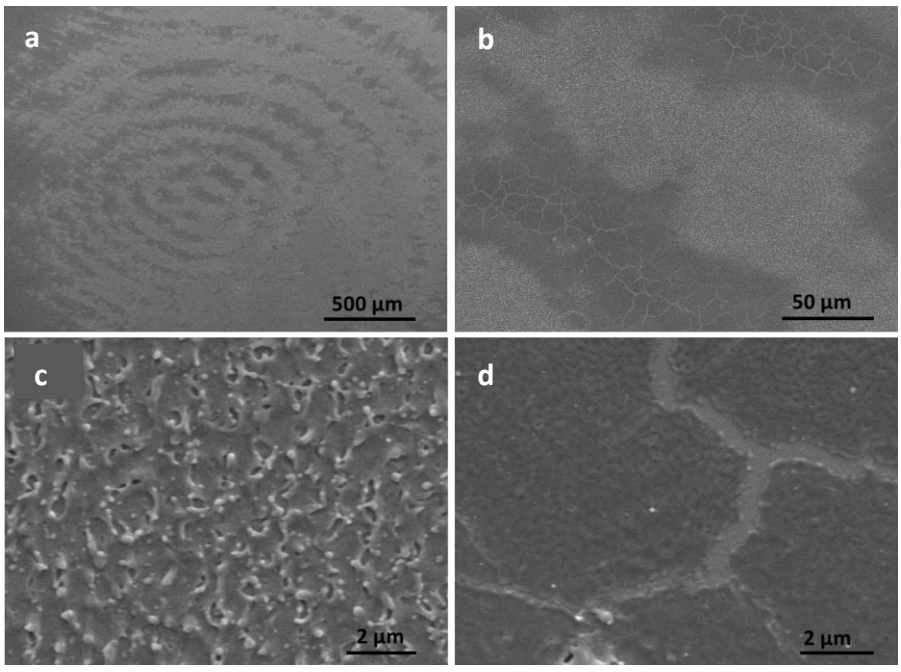

Figure 31. Surface evolution for picosecond laser treatment at 66 mJ for 5 pulses. (a) shows the overview of the irradiated area, b) shows the minima and maxima alternating behavior, c) shows the behavior in the white area corresponding to the maxima ring, and d) shows the microcracking in the dark area corresponding to the minima ring.

pulses. The overview of the irradiated area showed similar ringed behavior to the ns-LST result, though in this case the rings are solely due to the inherent minima and maxima of the laser mode. However, contrary to the ns-LST result, in this case there were morphological changes observed in both regions. The surface alternates between a melted surface showing evidence of initial stages of periodic ripple formation and a smoother melted layer developing microcracks. Nanoindentation of the laser treated samples, shown in Figure 32, shows a slight increase in hardness after 5 pulses that corresponds to the microcracked regions and regions near the edge of the irradiated zone.

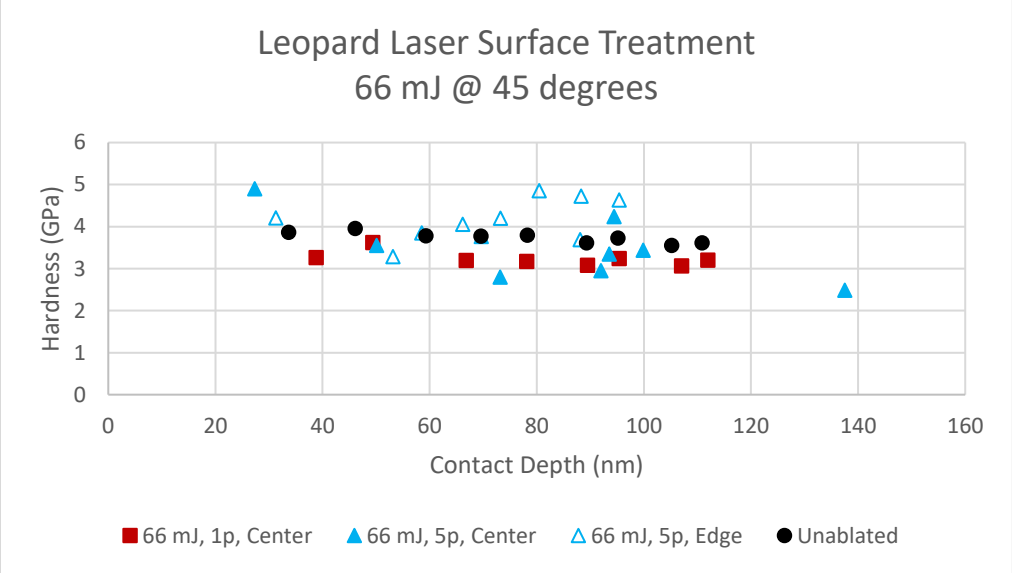

Figure 32. Hardness development after picosecond laser surface treatment with comparable parameters to previously completed nanosecond laser treatment.

While the hardness increase observed after ns-LST was more desirable, the localized nature of any morphological or mechanical changes was not desirable for the intended objective of applying this technique as a true surface treatment. The presence of two distinct alternating morphologies developed after ps-LST for the same conditions indicated that, while these particular parameters were not optimized for use with the picosecond laser, there was an increase in energy

acting on the surface in the minima rings. Additionally, there was a greater concentration of rings for the same irradiated area, reducing the distance between areas of similar behavior.

An effort was made to optimize the ps-LST conditions to achieve 3 goals: 1) maximize generation of intermetallic phases, 2) create a measurable intermixed layer in the Cu/Al system, and 3) reduce or eliminate microcracking of the surface. The spot size was fixed as 3.5 mm while pulse energy, angle of incidence, and pulse number varied according to the ranges identified in Table 2. Testing was completed on 500 nm thick Cu/Al with 25 nm layers and a 25 nm Ti capping layer over a range of conditions.

Table 2. Laser treatment parameters for testing with the Leopard ps laser

Parameter	**Test conditions**
Angle of incidence	45°, 55°, 67°
Pulse energy	25, 50, 75, 100 mJ
Pulse number	1-10, 20, 25, 50, 100-250

When considering intermetallic phase formation, the amount of energy absorbed by the material was a critical factor. For a fixed angle of incidence, either increasing the energy per pulse or the number of pulses were shown to generate a higher concentration of the Cu_9Al_4 intermetallic phase, as shown in Figure 33 and Figure 34. In particular, the combination of a 45° incidence angle with 5 pulses at 75 mJ results in a nearly complete shift of the base Cu peak to the Cu_9Al_4 peak. Figure 33 shows multiple spectra for the 45° incidence angle with 5 pulses at both 50 and 75 mJ that correspond to different test samples, demonstrating repeatability for samples tested under the same conditions. Altering the angle of incidence shows a much greater effect on the development of intermetallic phases. Testing at an oblique angle changes the reflectivity and absorptivity of a material coupled with a change in the spatial distribution and energy density

across the irradiated area. Additionally, laser treatment at high incidence angles reduces the likelihood of spallation of the film from high compressive stress propagation through the film. Samples tested at higher incidence angles survived laser treatment at higher energy or with significantly higher total pulses for lower energy tests, as can be seen in the 67° results shown in Figure 34b. However, the high pulse numbers, despite being two orders of magnitude higher than those in the 45° case, do not result in intermetallic phase precipitation. From the XRD results, the intermetallic phase precipitation was maximized for the 45° incidence angle.

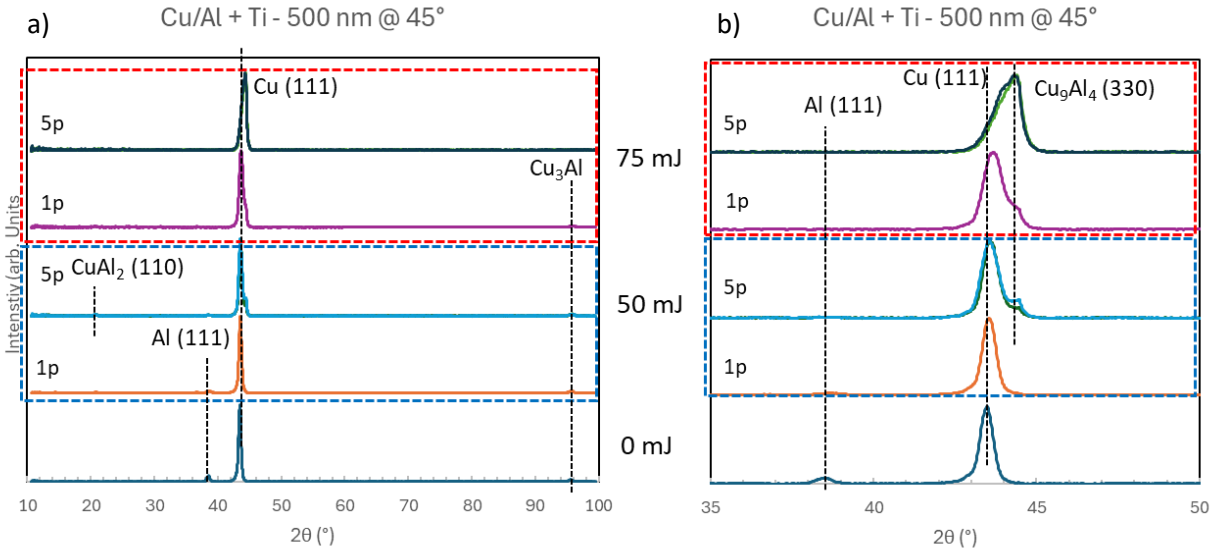

Figure 33. XRD spectra of as-deposited and laser-treated 500 nm Cu/Al + Ti at a 45° angle of incidence a) for the full standard 2θ range and b) a magnified view of the critical peaks. Testing done at 75 mJ is shown in the red boxes, and 50 mJ results are shown in the blue boxes.

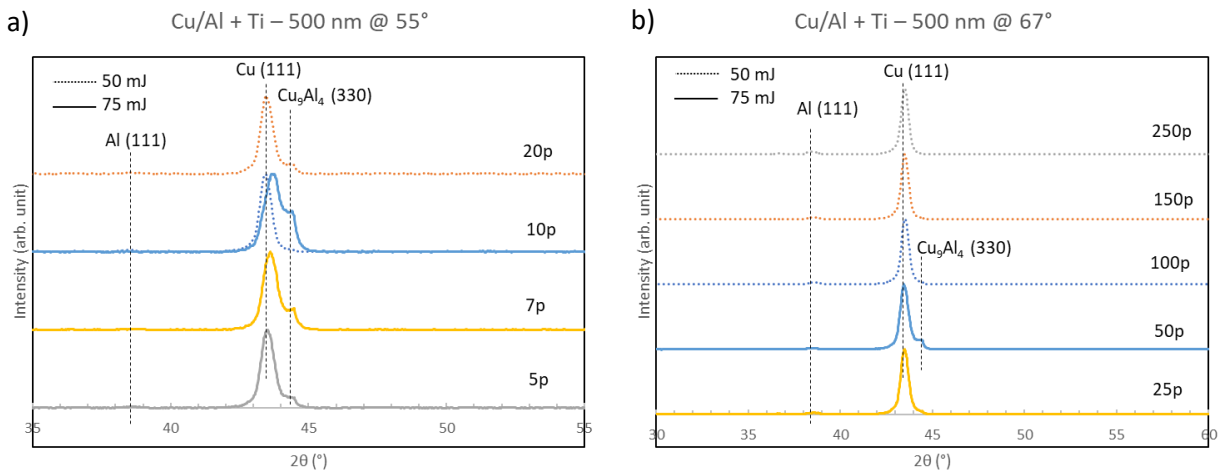

Figure 34. XRD spectra of laser-treated 500 nm Cu/Al + Ti for 50 and 75 mJ tests at a) 55° angle of incidence and b) 67° angle of incidence.

The surface morphology development of the 500 nm film after laser treatment at 45° with pulse energies of 50 mJ and 75 mJ resulted in a similar ringed structure of alternating minima and maxima positions. Lower energy or lower exposure regions (Figure 35b,e) progressively developed a vertical ripple pattern, while higher energy or higher exposure (Figure 35c, f) regions resulted in a higher degree of melting that eventually supersedes the ripple pattern. These surfaces generally had a much higher roughness compared to the microcracked surfaces present after ns-LST. However, examination of the cross-sectional morphology in Figure 36 showed the development of a clear intermixed layer after both 50 mJ and 75 mJ laser treatment. The 50 mJ treatment resulted in an intermixed layer ~140 nm thick and the intermixed layer thickness increases to ~175 nm with increasing pulse energy. One feature of note was the presence of voids commonly observed on the surface within the maxima rings and in the 75 mJ cross-section structure. The general evolution of the observed surface structures was sparse ripple formation, highly concentrated vertical ripple formation, lightly melted ripple formation, followed by a roughly melted surface with scattered voids. The presence of the many surface voids and the voids

present in the cross-section indicated the melted surface encapsulates the underlying ripple structure rather than fully replacing it, resulting in a porous surface layer.

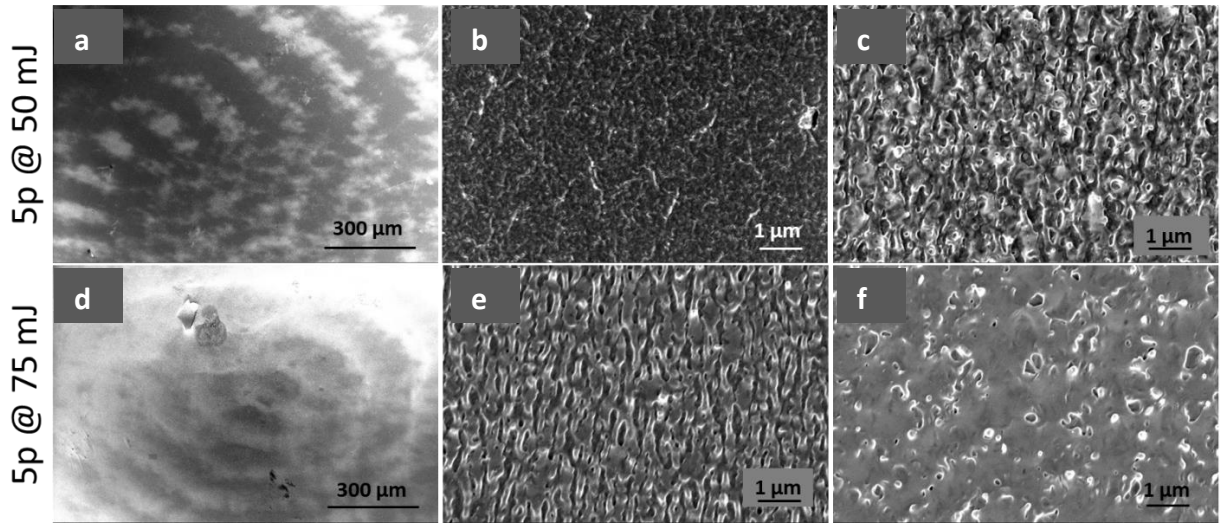

Figure 35. Surface evolution for picosecond laser treatment with 5 pulses at (a-c) 50 mJ and (d-f) 75 mJ. (a, d) show overviews of the irradiated area and resulting ring structure. (b, e) show the surface in the minima rings and (c, f) show the surface in the maxima rings.

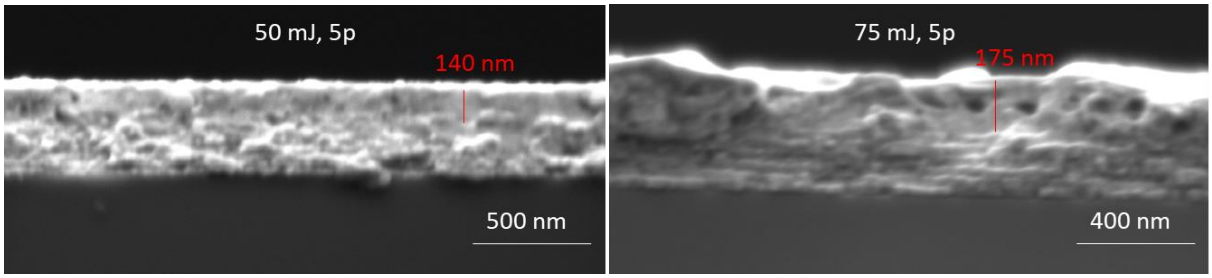

Figure 36. SEM of the cross-section of laser treated 500 nm Cu/Al + Ti showing formation of intermixed layers at the multilayer surface and the approximate intermixed layer thickness in red.

Despite the clear intermixed layers and presence of intermetallic phases for the 45° surface treatment conditions, the corresponding nanoindentation results showed relatively inconsistent strengthening compared to the as-deposited baseline. There was an increase in hardness for contact depths around 50 nm, corresponding to the first Cu/Al interface in the multilayer structure, after treatment with 50 mJ. However, for the 75 mJ case, while two tests show a significant increase in hardness, the majority of the indents result in mechanical properties that approach or fall below

the as-deposited mechanical response, despite showing more promising intermetallic generation. The surface roughness and porosity of the resulting intermixed layer were likely contributing factors to the disparity in the nanoindentation results.

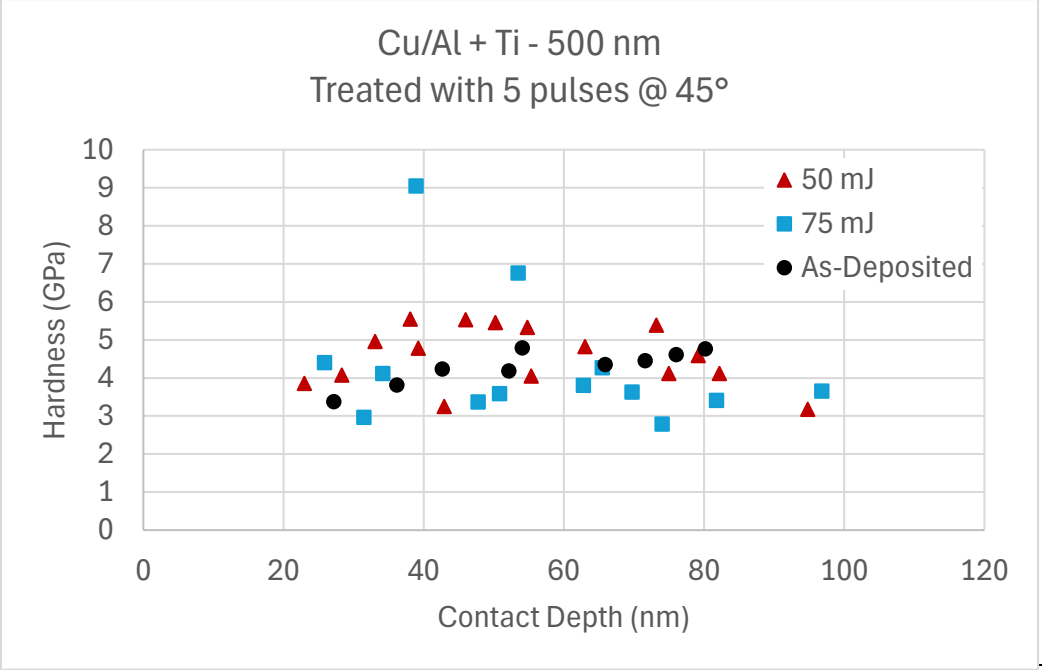

Figure 37. Hardness development of 500 nm Cu/Al + Ti after Leopard laser surface treatment with a 45° angle of incidence.

5.2.2 Objective 4: Simulated manufacturing conditions

In order for laser treatment for surface strengthening to be viable in industrial applications, the single-spot aspect of the testing described in the previous sections is not sufficient. In manufacturing conditions, the treatment would be applied to a wide swath of material, likely in either assembly line or moving laser configuration. Applying the laser treatment conditions over a large area rather than a single point introduced different requirements for success.

The first was expanding the laser treatment process over a two-dimensional area rather than a single test spot. To do this, a hexagonal array was implemented to maximize packing density and minimize untreated material between irradiated areas. The degree of overlap between

subsequent shots was set as 0%, 25%, or 50% in order to approximate the effect of the continuous scanning set up typically implemented at the industrial level. The overlap value was kept consistent in both x and y shifts of the array. The distance associated with the array overlap value was determined based on the spot size as measured at the testing pulse energy to avoid dead space in the array structure from reduced energy at the edges of the Gaussian laser distribution. Testing the array structure on laser burn paper as shown in Figure 38 revealed the effect the array overlap had on the treatment uniformity. Areas that were exposed to the laser treatment multiple times due to the overlapping shots become white with subsequent irradiation. From this result, the 0% and 50% overlap cases were preferable for generating a uniform treatment.

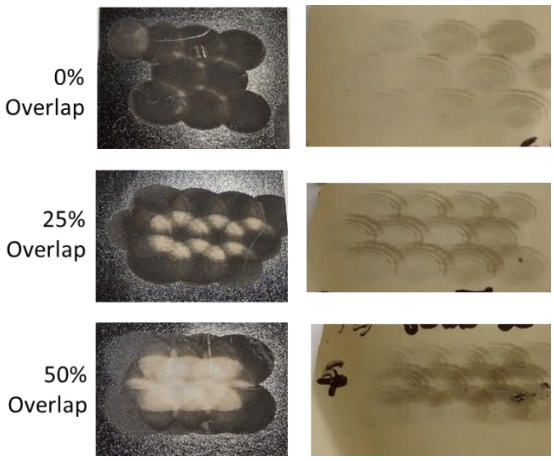

Figure 38. The hexagonal array structure for varying overlap distance shown on (left) laser burn paper and (right) 500 nm Cu/Al + Ti surface. The white areas on the burn paper show the repeated exposure of those locations due to the overlap structure.

The second consideration was single- versus multi-pulse processing of the surface. Many of the test cases presented here required multiple pulses to accumulate the energy needed to initiate strengthening through diffusion, intermixing, or intermetallic precipitation. However, multiple pulse treatment can result in undesirable thermal effects due to high repetition rates or undesired physical structuring of the surface that can change how the incident energy interacts with the surface. Single pulse processing is simpler and avoids these potential issues. In order to achieve

the same energy conditions in a single pulse, the energy density needs to increase. From the baseline conditions of 50 mJ laser treatment at 45°, the energy density was increased utilizing two methods: 1) increasing the pulse energy to 75 mJ, or 2) decreasing the incidence angle to 30°.

Though the previous nanoindentation results for a single location showed an increase in hardness for 50 mJ testing at 45° (Figure 37), when applied in the array testing conditions, the nanoindentation results showed no significant increase in hardness (Figure 39a-b). Increasing the energy to 75 mJ resulted in an increase in hardness particularly for shallow contact depths for film thickness of both 500 nm and 1 μm (Figure 39c, d). Both the 50 mJ and 75 mJ test cases exhibited the development of an intermixed layer as shown in Figure 40 and the thickness of the intermixed layer increases with increasing pulse energy despite requiring less pulses. Similarly, nanoindentation analysis of array testing completed at a 30° incidence angle (Figure 41) showed much more consistent increases in hardness, particularly when the contact depth was around 40 – 60 nm, which would correspond to the area around the first Cu/Al interface in the as-deposited material. For both the 45°/75 mJ and 30°/50 mJ cases, regardless of total film thickness, a single-pulse laser treatment option resulted in an increase in hardness. The single pulse with 50% overlap cases consistently showed increases in the mechanical properties, which were the cases most likely to approximate a continuous raster process in industry. XRD spectra shown in Figure 42 for the single pulse arrays for both the 45°/75 mJ and 30°/50 mJ cases showed the formation of the Cu_9Al_4 intermetallic phase for several sets of laser treatment conditions. Unsurprisingly, the 50% overlap conditions resulted in stronger intermetallic peaks, though interestingly, for the 45°/75 mJ case the 500 nm film thickness resulted in a more significant shift to the Cu_9Al_4 peak, while the 1 μm film thickness shifts more drastically in the 30°/50 mJ case.

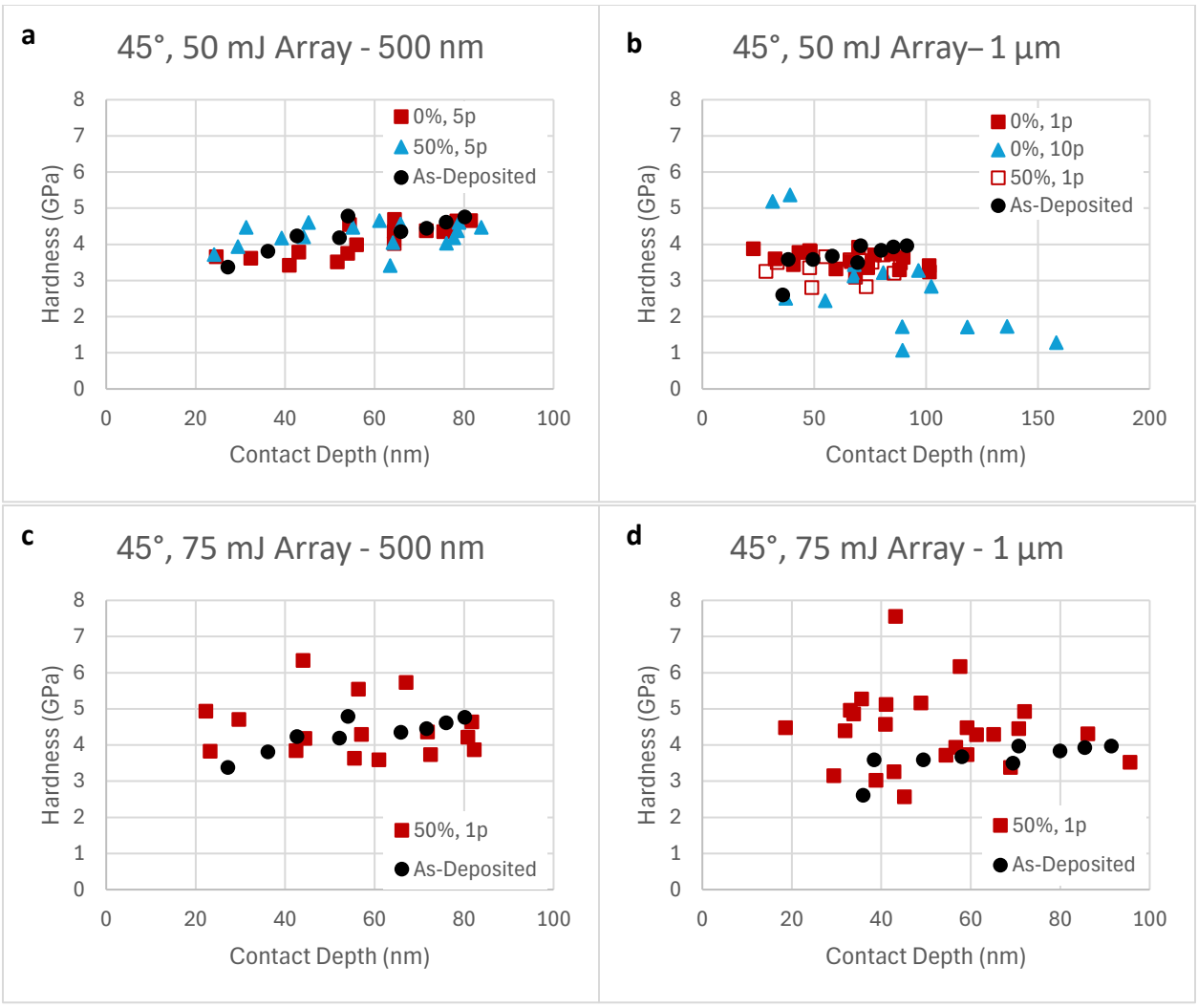

Figure 39. Hardness distribution with contact depth after array laser treatment with 45° incidence angle at a) 50 mJ on 500 nm Cu/Al, b) 50 mJ on 1 µm Cu/Al, c) 75 mJ on 500 nm Cu/Al, and d) 75 mJ on 1 µm Cu/Al.

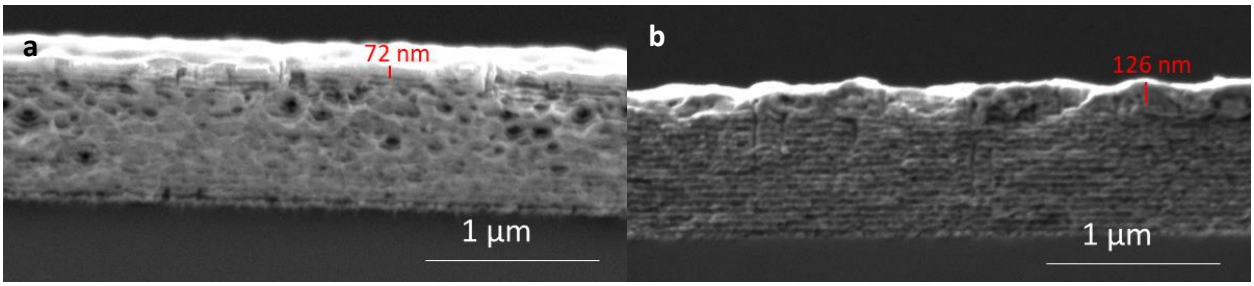

Figure 40. Cross-sectional morphology after array laser treatment for 1 µm Cu/Al at 45° with a) 5 pulses at 50 mJ with 0% overlap and b) 1 pulse at 75 mJ with 50% overlap.

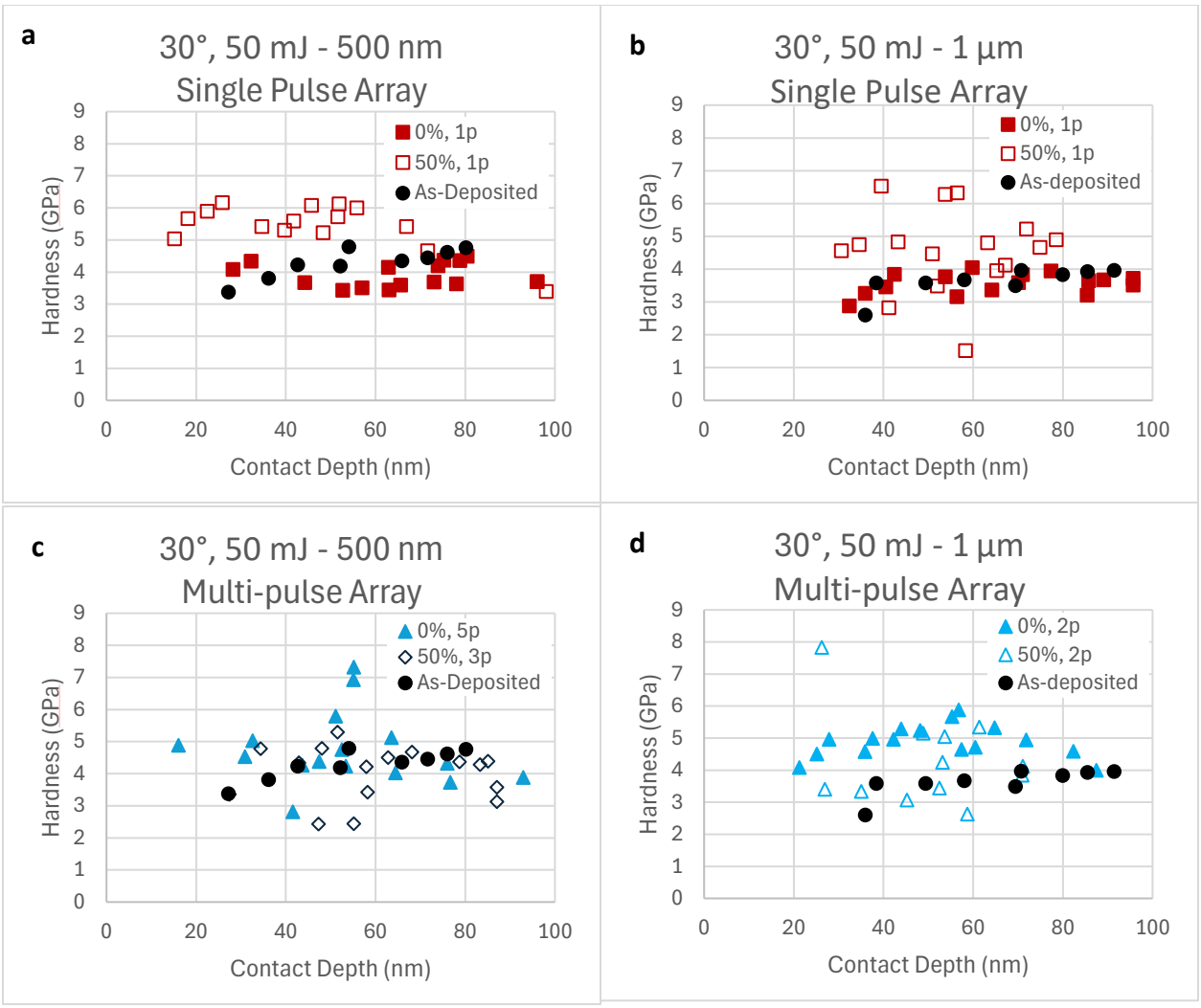

Figure 41. Hardness distribution with contact depth after array laser treatment with 30° incidence angle at 50 mJ after a) one pulse per position on 500 nm Cu/Al, b) one pulse per position on 1 µm Cu/Al, c) multiple pulses per position on 500 nm Cu/Al, and d) multiple pulses per position on 1 µm Cu/Al.

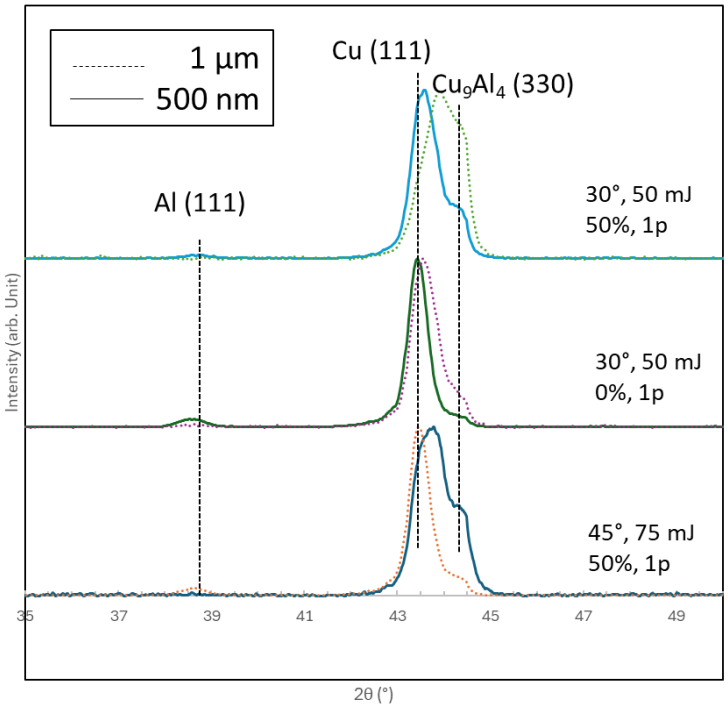

Figure 42. XRD spectra of laser treated Cu/Al + Ti for various single pulse array conditions for 1 µm and 500 nm films.

For both 500 nm and 1 µm film thicknesses shown in Figure 43, a measurable intermixed layer formed with a thickness ranging from 120 nm to 200 nm depending on the treatment conditions. Due to the Gaussian laser profile and the array treatment conditions, the thickness of the intermixed layers were not consistent across the irradiated area, as evidenced by Figure 43d and Figure 44, which show two locations within the array treatment area but the layered structure was still partially visible near the surface of the film. Additionally, the cross section in Figure 44 showed an interesting phenomenon in the top third of the film thickness. Along the length of the cross-section, there were many small vertical channels from the film surface through several layers of the film, an example of which is indicated by the red circle. The presence of these channels coupled with the voids present in the intermixed layers supports the theory that when the film

surface initially melts as a result of higher energy density, the melted surface encapsulated the previously formed ripple structure, creating a porous layer at the surface.

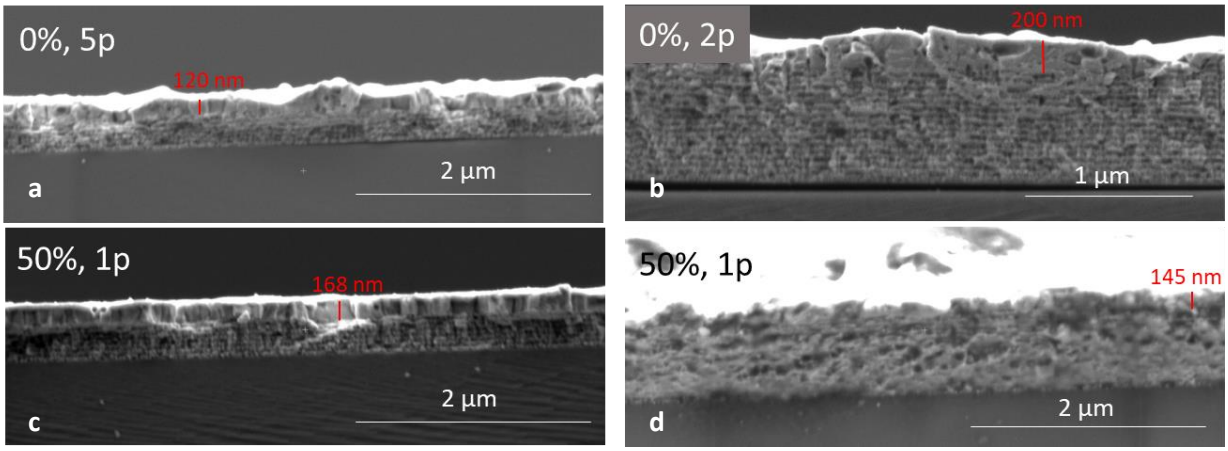

Figure 43. SEM of the cross-section of (left) 500 nm and (right) 1 µm Cu/Al + Ti after Leopard laser treatment at 30°/50 mJ showing the formation of an intermixed layer and the approximate intermixed layer thickness in red.

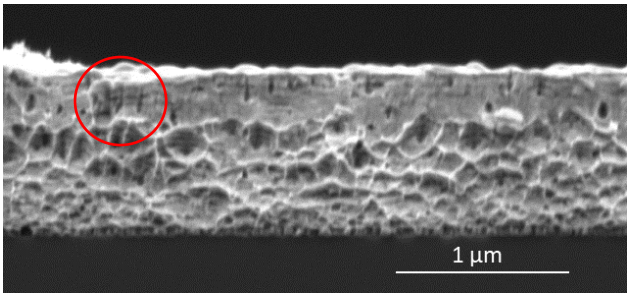

Figure 44. SEM of the cross-section of 1 µm Cu/Al + Ti after Leopard laser treatment at 30°/50 mJ/0%/2p showing the variation in intermixed layer formation as compared to Figure 43b and the formation of vertical channels as a precursor to surface porosity as indicated by the red circle.

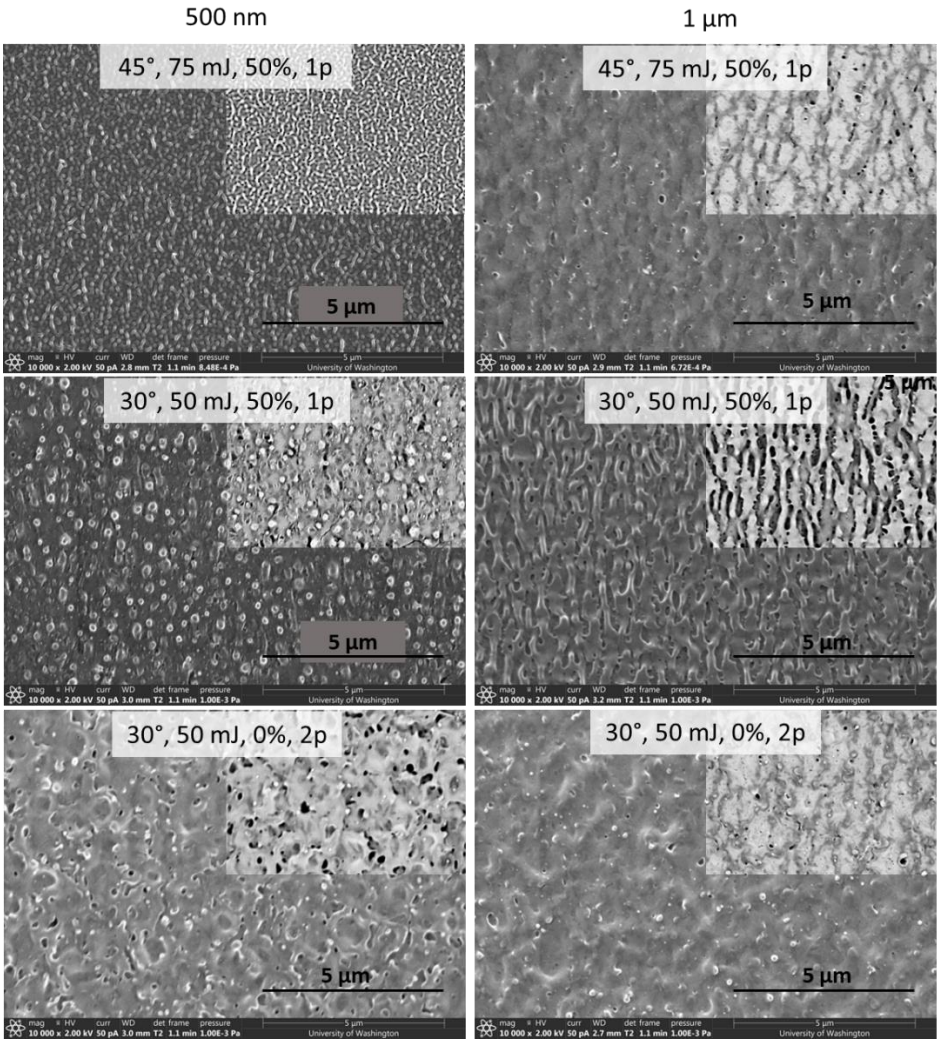

Figure 45. Surface morphologies after array laser treatment for a range of higher energy density conditions. Results for the 500 nm thick Cu/Al are on the left and 1 µm results are on the right. The main SEM images are secondary electron images where contrast shows topography, while the inset images are backscatter detection images of the same location where contrast shows relative elemental composition.

Comparing the surface morphologies for the array conditions resulting in the clearest increases in hardness, shown in Figure 45, the surface morphology was consistently past the initiation of vertical, optically dominated periodic structures, and most often clearly in the melted surface phase. This further supports the need for higher energy to generate the intermixed layer and intermetallic phases required for strengthening. Additionally, two different sets of laser treatment conditions, 45°/75 mJ/50%/1p and 30°/50 mJ/0%/2p resulted in developing an extremely

similar surface morphology, which indicates a flexibility in the laser treatment design to achieve similar results.

6. Summary

6.1 Objective 1: Laser energy effect

Laser treatment of Ti/Ni resulted in the development of an intermixed surface layer, the thickness of which increased with increasing laser energy. When the intermixed layer thickness grew to the full thickness of the film, additional energy promotes extreme melting of the film and leads to the formation of voids and bubble within the material. This indicates the intermixed surface development is dominated by thermal diffusion during treatment. Laser irradiation induces ultra-high temperatures on the surface, but the thermal effects are confined to a shallow depth, resulting in the formation of the intermixed region.

Intermixing alone is not sufficient to affect the surface strength of the Ti/Ni films, as the intermixed layer is present after treatment pulse energies ≤ 50 mJ, but there is no corresponding change in hardness for those cases. With the onset of intermetallic phases within the intermixed layer, an increase in hardness can be observed. The development of intermetallic phases with respect to pulse energy indicates a critical activation energy to initiate intermetallic formation, and the increase in the range of intermetallic phases with further increase in energy indicates the improved diffusion mobility with higher energy. As the concentration of intermetallic phases increases, there is a subsequent increase in hardness.

Additionally, periodic surface structures were observed in lower energy conditions that were not dominated by melting. There was no associated change in hardness with the onset of the structured surfaces.

6.2 Objective 2: Layer and film thickness effects

Increasing the layer thickness leads to an increase in the energy accumulation at the surface. Between Ti/Ni films with 20 nm layer and 50 nm layers, the 50 nm case developed partial and fully intermixed layers at lower pulse energies. Additionally, the surfaces for the 50 nm case are highly melted compared to the relatively smooth and uniform surface development seen in the 20 nm case. While intermetallic formation occurs under both conditions, the specific intermetallic phases that form are different. The increased energy in the 50 nm case likely promotes more mobility of the Ni into Ti-rich layers, resulting in the formation of $NiTi_2$, as opposed to the NiTi phase observed first in the 20 nm case.

Increasing the film thickness from 500 nm to 1 μm, the intermixed layer development trend regardless of layer thickness is similar to the 20 nm/500 nm case, with initially a thin intermixed layer characterized by smooth, periodic surface structures. Increasing pulse energy led to increased thickness of the intermixed layer, but there were no intermetallic phases formed and no corresponding increase in hardness. This indicates that the energy accumulation never reached the critical level required to precipitate those phases, even after testing with 100 mJ. This is likely due to the increased number of interfaces through the 1 μm thickness, which will affect the thermal energy dissipation through the film. Thin layers and larger numbers of interfaces will lead to more energy dissipation, reducing the energy accumulation at the intermixed region. Larger overall film thickness also has longer heat conduction distance, further reducing energy accumulation.

6.3 Objective 3: Surface intermetallic precipitation in Cu/Al

Annealed Cu/Al has shown the potential dramatic increase in strength possible for Cu/Al material systems due to intermetallic formation after heat treatment. The results from laser treatment of Ti/Ni multilayers, summarized in Objectives 1 and 2, show the application of laser

surface treatment for localized hardness increases due to intermetallic precipitation in Ti/Ni. However, the extremely high reflectivity of Cu and Al at 1064 nm introduces a unique challenge in adapting laser surface treatment with similar conditions to the Cu/Al thin film system. A 25 nm thick Ti absorbing layer was added to the surface of the Cu/Al multilayer structure to improve the absorption of the incident energy from the laser. With this added layer, there is a visible improvement in energy absorption at the film surface, however, due to the difference in thermal properties between Ti and Al, a phenomenon of microcracking is observed in the Ti layer after laser treatment.

Laser treatment of the 1 μm Cu/Al + Ti material system was conducted using lasers with different pulse durations: a 5 ns pulse and a 120 ps pulse. After laser treatment, both cases result in a ringed structure of alternating minima and maxima from interference either inherent to the laser mode or due to passing through an aperture. After laser treatment with the nanosecond pulse laser, while the surface in the minima regions behaves consistent with the as-deposited behavior, in the maxima regions microcracking of the Ti layer is observed as well as evidence of a melted Ti layer that is covered in void and bubbles for even single pulses but melted smooth as the number of pulses increases. However, this melted surface is confined to the Ti layer as the resulting film shows no intermixing and the development of only a small Cu_9Al_4 peak although the thermal penetration depth is over 1 μm. This is likely due to the comparatively low thermal conductivity of Ti compared to the much higher thermal properties for Al and Cu. Despite the low concentration of intermetallic phases, nanoindentation shows a dramatic increase in hardness for shallow indents that decay to the as-deposited mechanical properties as contact depth increases. In contrast, laser treatment with the picosecond pulse laser shows the onset of a periodic ripple structure evolving into a melted structure that forms at two different rates depending on if the location is in the minima

and maxima regions. With a much shallower thermal penetration depth of approximately 225 nm, there is the formation of a measurable intermixed layer and the precipitation of intermetallic phases. The picosecond laser testing results in clearer intermetallic generation according to XRD results though the corresponding nanoindentation shows a more consistent but muted increase in hardness. The surface roughness after picosecond laser treatment is much higher compared to the smooth melted surface after nanosecond laser treatment which contributes to a much larger error in nanoindentation results. Intermetallic phase precipitation in Cu/Al is optimized with higher energy density on the film surface, therefore lower angles of incidence at lower pulse energy and pulse number are preferable despite the ability of the film to survive extremely high pulse numbers at high angles of incidence.

6.4 Objective 4: Manufacturing conditions

In order to be viable in manufacturing applications, the laser surface treatment needs to be applicable over a wide area, not a single spot. Overlapping and thermal accumulation from multiple shots are key considerations to control the intermixed layer thickness and intermetallic phase formation uniformly over the entire treated area. A hexagonal array structure was implemented to maximize the packing density of elliptical spot profiles due to the oblique angle of incidence. Three overlap conditions were tested: 0%, 25%, and 50% overlap in x and y directions. The 0% and 50% overlap conditions maximized potential surface uniformity of energy exposure, though not necessarily uniform surface morphological development. Array conditions were tested with a range of picosecond laser treatment parameters, but in order to reduce the disadvantages associated with multiple pulse processing, arrays created with higher energy density (either 45°/75 mJ or 30°/50 mJ) showed intermetallic phase generation and a corresponding increase in hardness with single-pulse arrays. However, the surface roughness as well as the

variety of surface morphological zones from competing interference of each pulse on the surface development results in a non-uniform distribution of mechanical properties across the irradiated areas.

6.5 Future perspectives

In this work, the effectiveness of laser surface treatment for targeted strengthening was dependent on a number of factors, from laser parameters like pulse energy, angle of incidence, and laser pulse duration to material parameters including layer thickness, total film thickness, and the optical and thermal properties of the base materials which govern the efficiency of the energy absorption and distribution within the multilayer. The development of a predictive model or simulation to determine the most effective parameters for a combination of pulsed laser and material system based on the optical and thermal properties would be invaluable when designing new experiments. Additionally, the studies included in this work center around using laser surface treatment to locally change mechanical properties to suit a strength-based objective. However, laser surface treatment can be used for targeted alloying of the surface to locally change other properties, such as electrical conductivity or thermal conductivity depending on the material system it is applied to.

Further extensions of the laser-induced targeted surface strengthening objective include improving the uniformity of the surface treatment results. Additionally, characterizing the effect of laser treatment on other surface mechanical properties such as wear resistance could have potential applications in improving the life of microscale devices. Finally, there is an opportunity to use laser surface treatment on more complex material systems to further tailor the mechanical property response. For example, coupling laser surface treatment with a gradient thickness

multilayer thin film or strategically inserting low thermal conductivity materials in a multilayer of high thermal conductivity to control heat conduction through the film thickness.

7. References

[1] S. P. Wen, R. L. Zong, F. Zeng, Y. L. Gu, Y. Gao, and F. Pan, "Thermal stability of microstructure and mechanical properties of Ni/Ru multilayers," *Surface and Coatings Technology,* vol. 202, pp. 2040-2046, 2008/02/15/ 2008.

[2] Z. Yang and J. Wang, "Coupled annealing temperature and layer thickness effect on strengthening mechanisms of Ti/Ni multilayer thin films," *Journal of the mechanics and physics of solids,* vol. 88, pp. 72-82, 2016.

[3] X. Li, L. Lu, J. Li, X. Zhang, and H. Gao, "Mechanical properties and deformation mechanisms of gradient nanostructured metals and alloys," *Nature Reviews Materials,* vol. 5, pp. 706-723, 2020/09/01 2020.

[4] S. Petrović, B. Radak, D. Peruško, P. Pelicon, J. Kovač, M. Mitrić, B. Gaković, and M. Trtica, "Laser-induced surface alloying in nanosized Ni/Ti multilayer structures," *Applied Surface Science,* vol. 264, pp. 273-279, 1/1/ 2013.

[5] N. Ahmad, J. Stokes, N. A. Fox, M. Teng, and M. J. Cryan, "Ultra-thin metal films for enhanced solar absorption," *Nano energy,* vol. 1, pp. 777-782, 2012.

[6] P. Whiteside, J. Chininis, and H. Hunt, "Techniques and Challenges for Characterizing Metal Thin Films with Applications in Photonics," *Coatings (Basel),* vol. 6, p. 35, 2016.

[7] A. Vereschaka, "Delamination and Longitudinal Cracking in Multilayered Composite Nanostructured Coatings and Their Influence on Cutting Tool Wear Mechanism and Tool Life," ed: IntechOpen, 2018.

[8] M. B. Daia, P. Aubert, S. Labdi, C. Sant, F. A. Sadi, P. Houdy, and J. L. Bozet, "Nanoindentation investigation of Ti/TiN multilayers films," *Journal of Applied Physics,* vol. 87, pp. 7753-7757, 2000.

[9] Z. G. Wu, G. A. Zhang, M. X. Wang, X. Y. Fan, P. X. Yan, and T. Xu, "Structure and mechanical properties of Al/AlN multilayer with different AlN layer thickness," *Applied surface science,* vol. 253, pp. 2733-2738, 2006.

[10] R. K. Lakkaraju, F. Bobaru, and S. L. Rohde, "Optimization of multilayer wear-resistant thin films using finite element analysis on stiff and compliant substrates," *Journal of vacuum science & technology. A, Vacuum, surfaces, and films,* vol. 24, pp. 146-155, 2006.

[11] L. Elias, K. U. Bhat, and A. C. Hegde, "Development of nanolaminated multilayer Ni–P alloy coatings for better corrosion protection," *RSC advances,* vol. 6, pp. 34005-34013, 2016.

[12] J. Y. Zhang, F. L. Zeng, K. Wu, Y. Q. Wang, X. Q. Liang, G. Liu, G. J. Zhang, and J. Sun, "Size-dependent plastic deformation characteristics in He-irradiated nanostructured Cu/Mo multilayers: Competition between dislocation-boundary and dislocation-bubble interactions," *Materials science & engineering. A, Structural materials : properties, microstructure and processing,* vol. 673, pp. 530-540, 2016.

[13] A. Misra, M. J. Demkowicz, X. Zhang, and R. G. Hoagland, "The radiation damage tolerance of ultra-high strength nanolayered composites," *JOM (1989),* vol. 59, pp. 62-65, 2007.

[14] P. F. Bloser, F. Shirazi, O. Echt, J. E. Krzanowski, J. S. Legere, M. L. McConnell, J. G. Tsavalas, E. N. Wong, and P. H. Aliotta, "A concept for a soft gamma-ray concentrator using thin-film multilayer structures," pp. 99056L-99056L-12.

[15] C. Garlisi, E. Trepci, X. Li, R. Al Sakkaf, K. Al-Ali, R. P. Nogueira, L. Zheng, E. Azar, and G. Palmisano, "Multilayer thin film structures for multifunctional glass: Self-cleaning, antireflective and energy-saving properties," *Applied energy,* vol. 264, p. 114697, 2020.

[16] K. Kobayashi, K. Yamaguchi, M. Hayakawa, and M. Kimura, "High-temperature fatigue properties of austenitic superalloys 718, A286 and 304L," *International Journal of Fatigue,* vol. 30, pp. 1978-1984, 2008 2008.

[17] J. Azadmanjiri, C. C. Berndt, J. Wang, A. Kapoor, V. K. Srivastava, and C. Wen, "A review on hybrid nanolaminate materials synthesized by deposition techniques for energy storage applications," *Journal of materials chemistry. A, Materials for energy and sustainability,* vol. 2, pp. 3695-3708, 2014.

[18] S. Park, U. Han, D. Choi, and J. Hong, "Layer-by-layer assembled polymeric thin films as prospective drug delivery carriers: design and applications," *Biomaterials research,* vol. 22, pp. 29-29, 2018.

[19] L. Weisensel, F. Mueller, N. Travitzky, and P. Greil, "Microstructure and mechanical properties of AlN/Al-Si multilayer composites fabricated by reactive melt infiltration technique," *Journal of Materials Science Letters,* vol. 22, pp. 721-724, 2003/05/01 2003.

[20] Y. Chen, Y. Liu, C. Sun, K. Y. Yu, M. Song, H. Wang, and X. Zhang, "Microstructure and strengthening mechanisms in Cu/Fe multilayers," *Acta materialia,* vol. 60, pp. 6312-6321, 2012.

[21] B. C. Kang, H. Y. Kim, O. Y. Kwon, and S. H. Hong, "Bilayer thickness effects on nanoindentation behavior of Ag/Ni multilayers," *Scripta materialia,* vol. 57, pp. 703-706, 2007.

[22] Y. Liu, D. Bufford, H. Wang, C. Sun, and X. Zhang, "Mechanical properties of highly textured Cu/Ni multilayers," *Acta materialia,* vol. 59, pp. 1924-1933, 2011.

[23] J. Y. Zhang, Y. Liu, J. Chen, Y. Chen, G. Liu, X. Zhang, and J. Sun, "Mechanical properties of crystalline Cu/Zr and crystal–amorphous Cu/Cu–Zr multilayers," *Materials science & engineering. A, Structural materials : properties, microstructure and processing,* vol. 552, pp. 392-398, 2012.

[24] X. Zhang, A. Misra, H. Wang, T. D. Shen, J. G. Swadener, J. D. Embury, H. Kung, R. G. Hoagland, and M. Nastasi, "Strengthening mechanisms in nanostructured copper/304 stainless steel multilayers," *Journal of materials research,* vol. 18, pp. 1600-1606, 2003.

[25] X. Y. Zhu, J. T. Luo, F. Zeng, and F. Pan, "Microstructure and ultrahigh strength of nanoscale Cu/Nb multilayers," *Thin solid films,* vol. 520, pp. 818-823, 2011.

[26] T. Ito, R. Yamamoto, and A. Yoshihara, "Mechanical properties of Cu/Al multilayered thin films," *Surface & coatings technology,* vol. 45, pp. 215-220, 1991.

[27] A. Misra, J. P. Hirth, and R. G. Hoagland, "Length-scale-dependent deformation mechanisms in incoherent metallic multilayered composites," *Acta materialia,* vol. 53, pp. 4817-4824, 2005.

[28] J. Wang, Q. Zhou, S. Shao, and A. Misra, "Strength and plasticity of nanolaminated materials," *Materials Research Letters,* vol. 5, pp. 1-19, 2017/01/02 2017.

[29] M. Nasim, Y. Li, M. Wen, and C. Wen, "A review of high-strength nanolaminates and evaluation of their properties," *Journal of materials science & technology,* vol. 50, pp. 215-244, 2020.

[30] Y. J. Ma, M. Z. Wei, C. Sun, Z. H. Cao, and X. K. Meng, "Length scale effect on the thermal stability of nanoscale Cu/Ag multilayers," *Materials science & engineering. A, Structural materials : properties, microstructure and processing,* vol. 686, pp. 142-149, 2017.

[31] K. Wu, J. Y. Zhang, P. Zhang, Y. Q. Wang, G. Liu, G. J. Zhang, and J. Sun, "Fracture behavior and adhesion energy of nanostructured Cu/Mo multilayer films," *Materials science & engineering. A, Structural materials : properties, microstructure and processing,* vol. 613, pp. 130-135, 2014.

[32] Z. Yang and J. Wang, "Thermo-mechanical stability and strengthening mechanisms of Ti/Ni multilayer thin films," [University of Washington Libraries], Seattle, 2016.

[33] Y. Zhou and J. Wang. (2024, Mechanical Properties of Thermally Annealed Cu/Ni and Cu/Al Multilayer Thin Films: Solid Solution vs. Intermetallic Strengthening. *Metals 14(3)*.

[34] X. Z. Wei, Q. Zhou, K. W. Xu, P. Huang, F. Wang, and T. J. Lu, "Enhanced hardness via interface alloying in nanoscale Cu/Al multilayers," *Materials Science and Engineering: A,* vol. 726, pp. 274-281, 2018/05/30/ 2018.

[35] S. Z. Shuja and B. S. Yilbas, "Laser induced heating of coated carbon steel sheets: Consideration of melting and Marangoni flow," *Optics and laser technology,* vol. 47, pp. 47-55, 2013.

[36] W. Pfleging, A. Ludwig, K. Seemann, R. Preu, H. Mäckel, and S. W. Glunz, "Laser micromachining for applications in thin film technology," *Applied surface science,* vol. 154, pp. 633-639, 2000.

[37] C. von der Heide, M. Grein, G. Bräuer, and A. Dietzel, "Methodology of selective metallic thin film ablation from susceptible polymer substrate using pulsed femtosecond laser," *Optics express,* vol. 28, pp. 33413-33432, 2020.

[38] A. Lasagni, C. Holzapfel, T. Weirich, and F. Mücklich, "Laser interference metallurgy: A new method for periodic surface microstructure design on multilayered metallic thin films," *Applied surface science,* vol. 253, pp. 8070-8074, 2007.

[39] E. Detemple, P. Leibenguth, C. Gachot, and F. Mücklich, "Large-area patterned formation of intermetallic phases on Ti/Al multilayer systems by laser interference metallurgy," *Thin solid films,* vol. 519, pp. 736-741, 2010.

[40] D. Perusko, J. Kovac, S. Petrovic, G. Drasic, M. Mitric, M. Milosavljevic, and J. Ciganovic, "Intermixing and phase transformations in Al/Ti multilayer system induced by picosecond laser beam," *Thin solid films,* vol. 591, pp. 357-362, 2015.

[41] S. Sinha, "Laser based surface treatment of bioactive glass: Dependence on pulsed laser ablation," *Applied Surface Science Advances,* vol. 11, p. 100295, 2022.

[42] A. Siozios, N. Kalfagiannis, D. V. Bellas, C. Bazioti, G. P. Dimitrakopulos, G. Vourlias, W. M. Cranton, E. Lidorikis, D. C. Koutsogeorgis, and P. Patsalas, "Sub-surface laser nanostructuring in stratified metal/dielectric media: a versatile platform towards flexible, durable and large-scale plasmonic writing," *Nanotechnology,* vol. 26, p. 155301, 2015.

[43] J.-F. Silvain, H. Niino, S. Ono, S. Nakaoka, and A. Yabe, "Surface modification of elastomer/carbon composite by Nd +:YAG laser and KrF excimer laser ablation," *Applied surface science,* vol. 141, pp. 25-34, 1999.

[44] E. L. Gurevich, "Mechanisms of femtosecond LIPSS formation induced by periodic surface temperature modulation," *Applied surface science,* vol. 374, pp. 56-60, 2016.

[45] P. Gregorčič, M. Sedlaček, B. Podgornik, and J. Reif, "Formation of laser-induced periodic surface structures (LIPSS) on tool steel by multiple picosecond laser pulses of different polarizations," *Applied Surface Science,* vol. 387, pp. 698-706, 2016/11/30/ 2016.

[46] L. T. Cangueiro, A. J. Cavaleiro, J. Morgiel, and R. Vilar, "Mechanisms of the formation of low spatial frequency LIPSS on Ni/ Ti reactive multilayers," *Journal of physics. D, Applied physics,* vol. 49, p. 365103, 2016.

[47] A. V. Dostovalov, V. P. Korolkov, and S. A. Babin, "Formation of thermochemical laser-induced periodic surface structures on Ti films by a femtosecond IR Gaussian beam: regimes, limiting factors, and optical properties," *Applied physics. B, Lasers and optics,* vol. 123, pp. 1-9, 2017.

[48] R. Moser, D. Seiler, H. P. Huber, and G. Marowsky, "Observation of a Spot Diameter Dependency in Confined Laser Ablation of Zinc Oxide on Copper-Indium-Diselenide," *Physics procedia,* vol. 56, pp. 1034-1040, 2014.

[49] T. Geldhauser, F. Ziese, F. Merkt, A. Erbe, J. Boneberg, and P. Leiderer, "Acoustic laser cleaning of silicon surfaces," *Applied physics. A, Materials science & processing,* vol. 89, pp. 109-113, 2007.

[50] P. Lorenz, M. Ehrhardt, and K. Zimmer, "Laser Structuring of Thin Layers for Flexible Electronics by a Shock Wave-induced Delamination Process," *Physics procedia,* vol. 56, pp. 1015-1023, 2014.

[51] L. Gemini, M. Hashida, Y. Miyasaka, S. Inoue, J. Limpouch, T. Mocek, and S. Sakabe, "Periodic surface structures on titanium self-organized upon double femtosecond pulse exposures," *Applied surface science,* vol. 336, pp. 349-353, 2015.

[52] G. Dumitru, V. Romano, H. P. Weber, M. Sentis, and W. Marine, "Femtosecond ablation of ultrahard materials," *Applied physics. A, Materials science & processing,* vol. 74, pp. 729-739, 2002.

[53] J. Gebauer, M. Burkhardt, V. Franke, and A. F. Lasagni, "On the Ablation Behavior of Carbon Fiber-Reinforced Plastics during Laser Surface Treatment Using Pulsed Lasers," *Materials,* vol. 13, p. 5682, 2020.

[54] B. Gaković, G. D. Tsibidis, E. Skoulas, S. M. Petrović, B. Vasić, and E. Stratakis, "Partial ablation of Ti/Al nano-layer thin film by single femtosecond laser pulse," *Journal of applied physics,* vol. 122, p. 223106, 2017.

[55] N. Farid, A. Sharif, P. D. Gupta, and G. M. O'Connor, "Selective laser ablation of molybdenum from aluminium in a multi-layered thin film system," *Surfaces and interfaces,* vol. 26, p. 101438, 2021.

[56] M. Čizmović, J. Kovač, M. Milosavljević, S. Petrović, G. Dražić, M. Mitrić, M. Obradović, P. Schaaf, and D. Peruško, "Intermixing in Al/Ti multilayer structures induced by nanosecond laser pulses," *Physica Scripta,* vol. 2013, p. 014008, 2013.

[57] M. S. Brown and C. B. Arnold, "Fundamentals of Laser-Material Interaction and Application to Multiscale Surface Modification," in *Laser Precision Microfabrication*, K. Sugioka, M. Meunier, and A. Piqué, Eds., ed Berlin, Heidelberg: Springer Berlin Heidelberg, 2010, pp. 91-120.

[58] M. R. Marks, K. Y. Cheong, and Z. Hassan, "A review of laser ablation and dicing of Si wafers," *Precision Engineering,* vol. 73, pp. 377-408, 2022/01/01/ 2022.

[59] W. C. Oliver and G. M. Pharr, "An improved technique for determining hardness and elastic modulus using load and displacement sensing indentation experiments," *Journal of Materials Research,* vol. 7, pp. 1564-1583, 1992.

[60] Z. Yang, M. Stossel, and J. Wang, "Microstructural evolution and surface strengthening of pulse-laser treated Ti/Ni multilayer thin films," *Extreme Mechanics Letters,* vol. 4, pp. 45-51, 2015.

[61] Z. Yang, M. Stossel, and J. Wang, "Thickness effect on microstructural and mechanical properties of pulse-laser treated Ti/Ni multilayer thin films," *Journal of Experimental Mechanics,* vol. 32, pp. 634-644, 2017.

[62] "CRC handbook of chemistry and physics (Online)," in *Chemical Rubber Company handbook of chemistry and physics*, Electronic ed. ed. Boca Raton, Fla: CRC Press, 1978.

Appendix

A.1. Effect of different optics on nanosecond pulsed laser treatment

The energy per pulse and the spot size determines the energy density of the laser treatment. Three different methods of controlling the spot size were implemented in the course of this study. The experimental setups for the three techniques are shown in Figure 46. The following work details the effects these methods have on the surface development and microstructural changes during Cu/Al laser treatment.

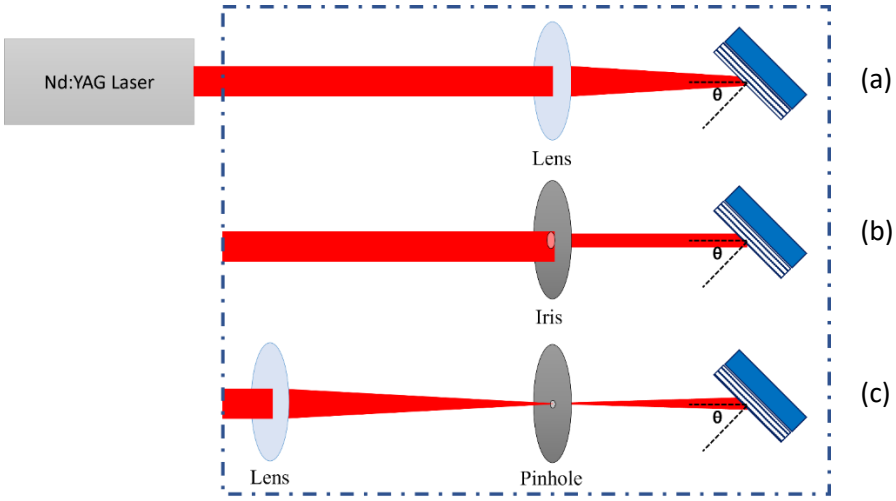

Figure 46. Experimental setup for the nanosecond pulse laser treatment used for processing the Cu/Al multilayer films. 3 different optics setups have been used in the course of this study: (a) optical focusing with a plano-convex lens, (b) mechanical filtering by selectively blocking portions of the beam with an iris aperture, (c) spatial filtering by focusing the beam through a pinhole and irradiating the sample with the diverging beam.

A.1.1. Optical Focusing

The most straightforward way to control spot size is to focus the laser through a plano-convex lens, as shown in Figure 46(a), and position the sample based on distance to achieve the desired spot diameter. The resulting surface development is dependent on the spatial distribution of the laser beam. In this case, the laser has a Gaussian distribution, maximizing energy in the center of the spot. It also resulted in a set of rings of alternating behavior corresponding to minima and maxima within the laser mode. Figure 47 shows the surface development for laser treatment

with a 4 mm spot size and 83 mJ pulse energy. This alternating behavior was not desirable due to the goal of creating uniform surfaces after laser treatment. In the minima rings, there was no change to the film morphology, microstructure, or properties when compared to an as-deposited sample. The maxima rings did exhibit an increase in hardness, but they are also the likely points of failure during laser testing. In particular, the upper left quadrant showed early delamination very consistently, though this was due to an inhomogeneity in the beam profile that was unique to this laser.

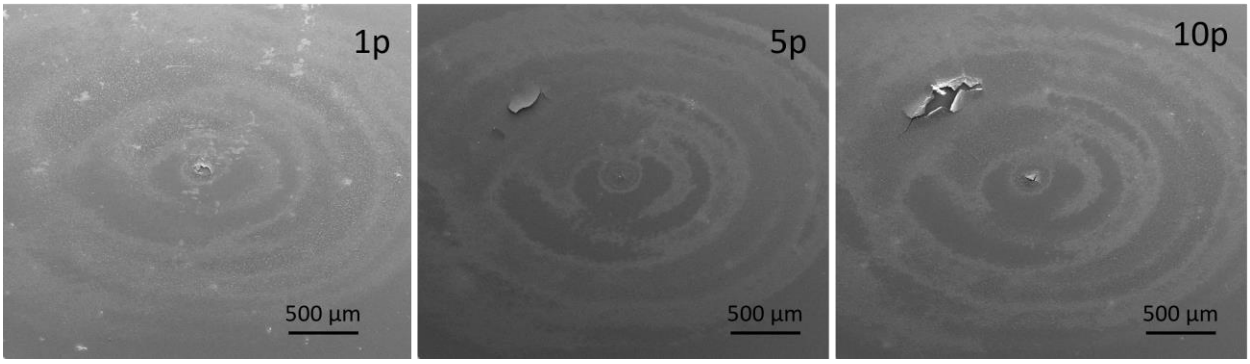

Figure 47 Surface development of Cu/Al after laser treatment with varying pulse number for 4 mm spot size, 83 mJ pulse energy.

Due to the ring structure observed after laser treatment, a specimen-labeling nomenclature has been introduced to clarify specifics of testing locations and spatial dependence trends. Figure 48 shows the labeling conventions applied here with regard to testing locations across the irradiated area. The ring or spot of irradiated material in the center is designated as R0, and each subsequent ring of irradiated material is labeled successively. The rings that show no obvious changes due to irradiation have been designated as “sub-rings” and are labels R1s, increasing in number as the distance from the center increases.

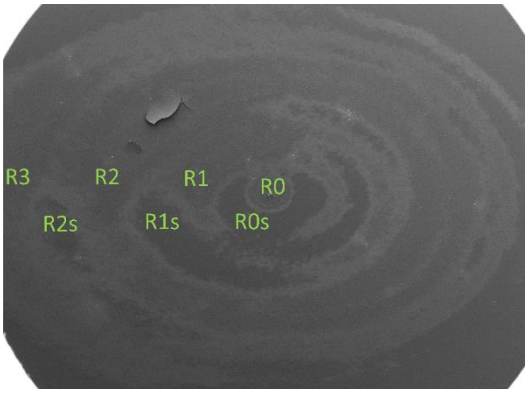

Figure 48. Specimen labeling nomenclature for orientation of test results with position on the sample.

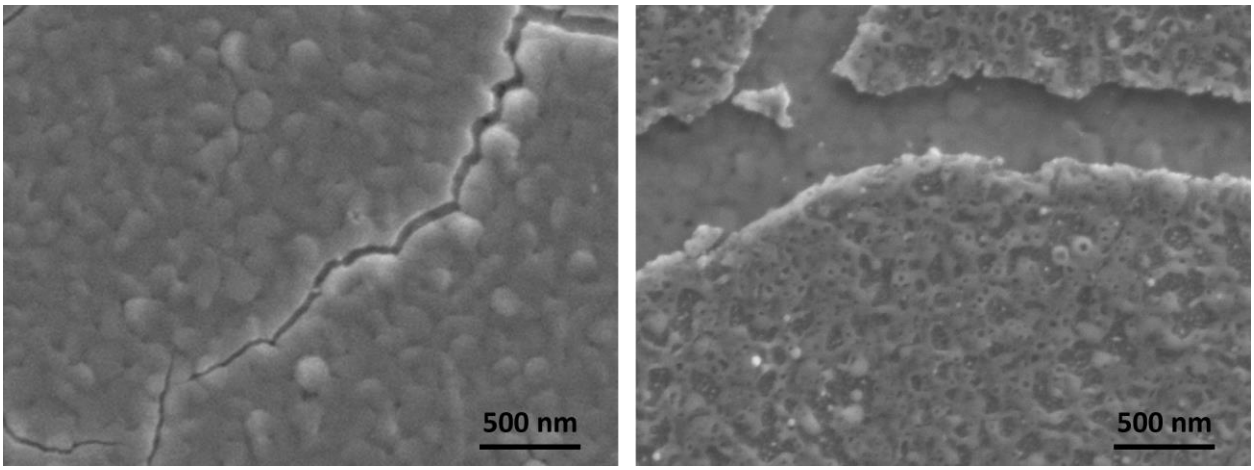

(a) (b)

Figure 49. Surface transition after 5 pulses from (a) uniform grain structure in R1s to (b) microcracked, melted Ti surface of bubbles and voids in R1, with preserved grain structure for exposed underlayer.

Figure 49 shows the transition of the surface from the functionally untreated zone R1s to the heavily exposed region of R1 after 5 pulses. In R1s, the film had the same uniform grain structure as an unablated sample. Moving towards the ring R1, a transition zone (Figure 49(a)) shows the encroachment of cracking among the grains. The crack tended to propagate along the grain boundaries, though there is some evidence of intragranular fracture as well. Figure 49(b) shows the rough melted surface in R1, covered in bubbles and voids. However, looking at the material exposed by the crack expansion, a smooth grain structure is observed, indicating the microcracking was due to thermal effects in the Ti layer that are not propagating into the bulk of the multilayer structure. This is further supported by the cross-sectional morphologies after 10

pulses (Figure 50). There was no evidence of intermixing even though there was significant thermal energy to cause the Ti film to melt. XRD spectra for the 1, 5, and 10 pulse cases were collected at different positions within the irradiated area but show no significant intermetallic formation or spatial dependence (Figure 51).

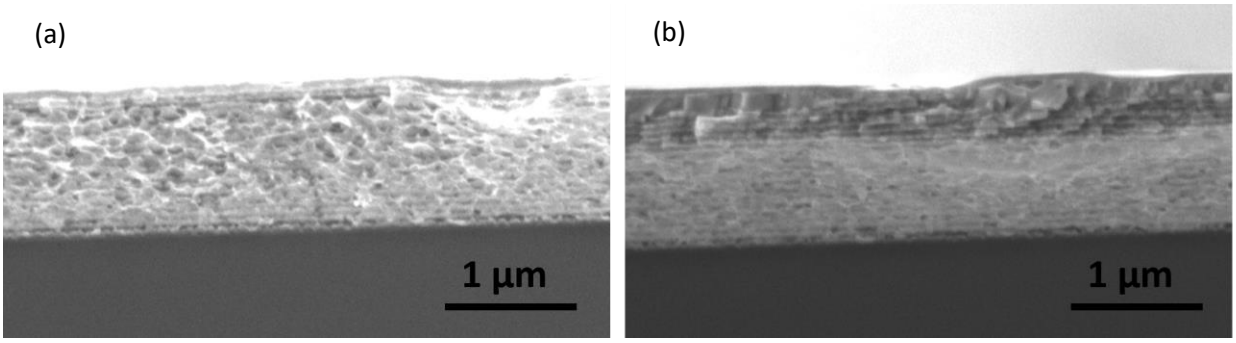

Figure 50. Cross-sectional SEM for (a) as-deposited and (b) laser-treated Cu/Al after 10 pulses at 83 mJ.

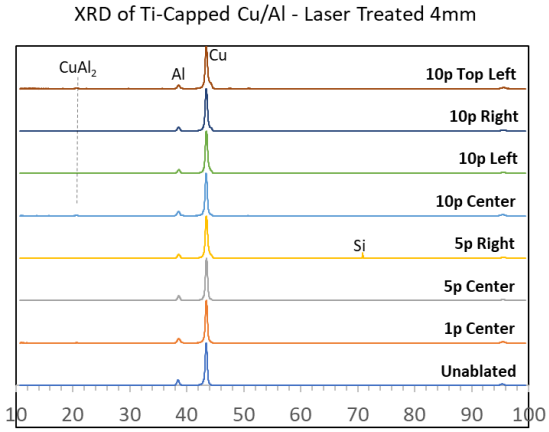

Figure 51. XRD spectra for laser-treated Cu/Al with respect to pulse number and relative position within the irradiated area.

A.1.2. Pinhole Spatial Filtering

Pinhole spatial filtering is a common method of homogenizing irregularities within a beam profile. To accomplish this, the beam is focused with a plano-convex lens to the minimum beam diameter and passed through a pinhole at the focal length of the lens, and diverging after passing

through that minimum point, as shown in Figure 46(c). Focusing through the pinhole blocks interference from competing modes of the laser and strips the resulting diffraction rings observed on the sample surface.

Applying pinhole filtering required some changes to the testing conditions. First, the maximum possible pulse energy is reduced from 275 mJ to 40 mJ, due to the laser passing through the minimum possible beam diameter. When the pulse energy is greater than 40 mJ, focusing to the minimum waist causes the energy density of the beam to ionize the air, creating a plasma that reduces the energy that can be deposited on the sample. Second, the angle of incidence was reduced to 30°. Initial tests with 40 mJ pulses at a 45° incidence angle resulted in no change to the surface or properties even after 150 pulses (Figure 52). Reducing the angle of incidence improves the absorption of the film, and changes in the surface of the film are apparent after 50 pulses. Figure 53 shows the surface evolution of the laser-treated films with no evidence of the interference rings on the surface. The local hot spot in the laser distribution plays a more substantial role in the morphology of the surface. The majority of the irradiation area shows a uniform surface that does not show any evolution in the hardness (Figure 54), while the area affected by the hot spot shows microcracking and a corresponding increase in hardness for high pulse numbers.

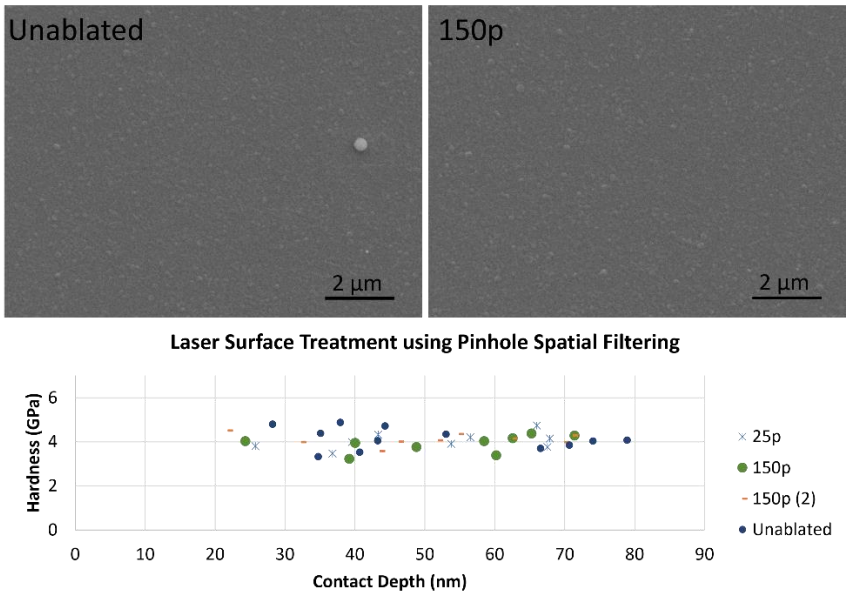

Figure 52. (a-b) Surface of Cu/Al for as deposited and spatially filtered laser-treated after 150 pulses with 45° angle of incidence shows no effect, confirmed by (c) hardness measurements showing no change in material properties up to 150 p.

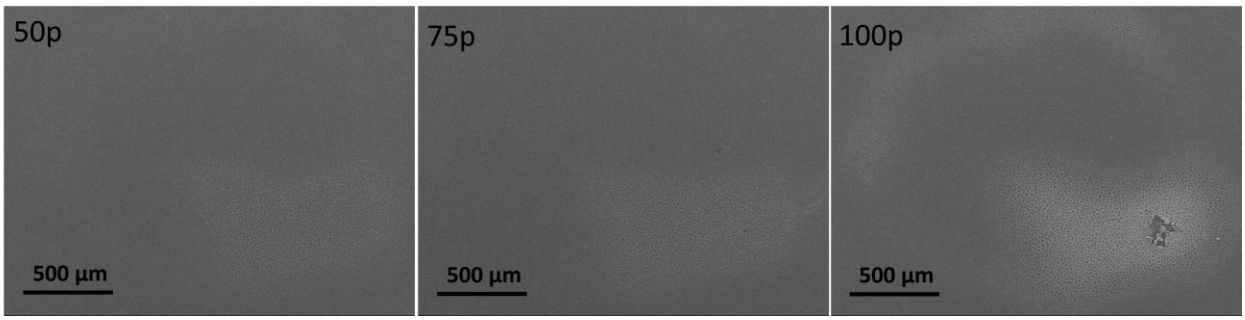

Figure 53. Surface development for spatially filtered laser treatment with 30° angle of incidence, showing surface morphology changes after 50 pulses, beginning in the bottom right area associated with the hot spot in the laser profile.

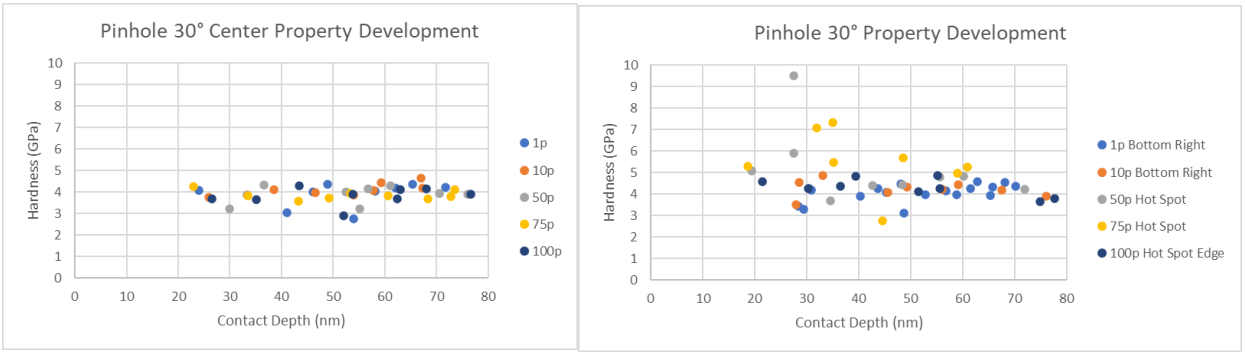

Figure 54. Hardness trends for pinhole filtered testing of Cu/Al with 30° angle of incidence showing no change in the properties in the center of the irradiated zone and increase in hardness within the higher exposure zone from the hot spot after 75 pulses.

A.1.3. Iris Mechanical Filtering

The presence of the hot spot in the laser profile and its subsequent effect on the localized failure of the film after laser treatment is quite problematic. When the film locally delaminates due to the energy concentration, the torn film acts as an edge effect for the region and film failure will continue to progress with subsequent pulses it may have otherwise survived until complete ablation of the film. Mechanical filtering, as illustrated in Figure 46(b) is simply physically blocking a portion of the laser beam to isolate the desirable portion of the beam profile that will interact with the film surface. In this case, an iris with an aperture of 3.5 mm was used to isolate the hot spot to prevent premature failure of the film. The light that passes through the iris is collimated and maintains the diameter of the aperture, thereby setting the spot size. Alternatively, the beam can be further shaped with focusing optics to changes the spot size following the same principle as discussed in Chapter A.1.1. Optical Focusing. The drawback of this method is the limitation on energy due to physically blocking the beam. For the nanosecond laser with a maximum energy of 275 mJ, after passing through the iris the maximum remaining energy is 66 mJ, which will be dependent on the size of the aperture, the initial beam diameter, and the spatial position of the aperture within the Gaussian profile.

As this set of conditions resulted in the most consistent results of the three methods described, the mechanical filtering method was selected as the main experimental set up when working with the nanosecond pulse laser. Therefore, the results of this configuration on surface strengthening are discussed in the main results section (5.2.1.2.1).

One factor not considered up to this point is the effect of the distance between the iris aperture and the sample. The laser has an inherent mode distribution that causes the ring behavior on the surface, and using the iris filtering method superimposed a secondary interference pattern

on the native ring formation due to diffraction as the light passes through the aperture. When the sample is far from the iris, the diffraction pattern expands into a few wide rings of affected and unaffected behavior which results in a consistent pattern, but not a uniform surface. By moving the sample closer to the iris, the rings do not disperse, leading to a surface of a multitude of thin rings packed close together, as seen in Figure 55. This has unique potential for homogenizing the surface morphology changes as the distinction between the affected and unaffected zones is less clearly defined. Nanoindentation of surfaces prepared with the iris 2 cm from the sample and 25 cm from the sample show that for the same laser treatment conditions, more energy was isolated in the wide distinct maxima bands of the 25 cm test case, leading to earlier intermixing behaviors. Alternatively, the 2 cm distance case may need increased conditions to promote higher energy accumulation but may result in a more uniform response when it occurs.

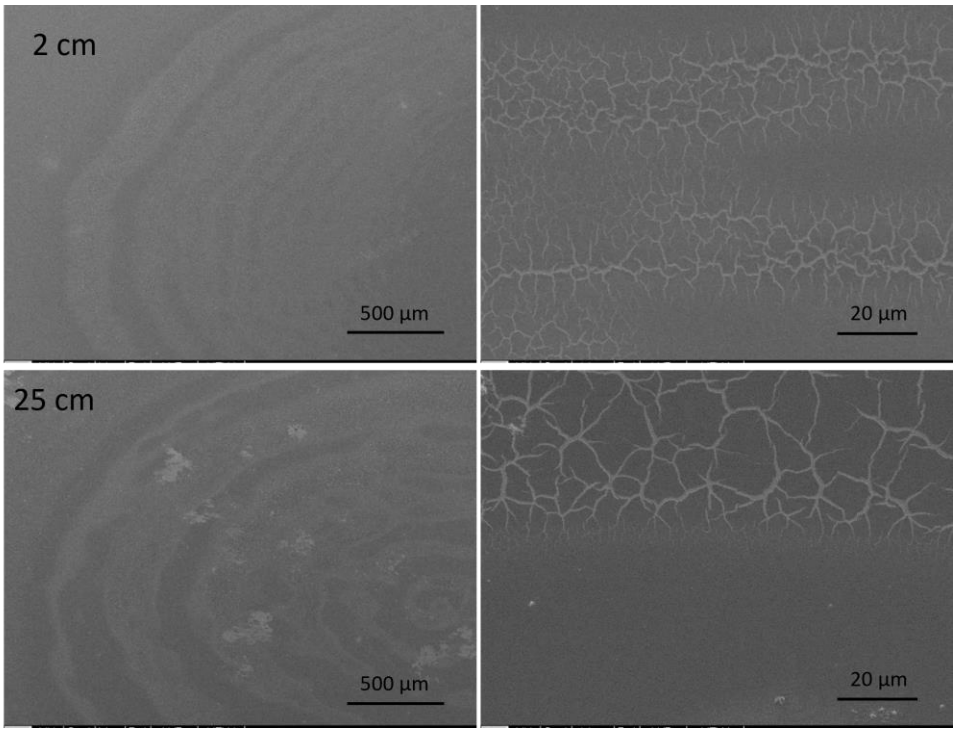

Figure 55. Surface development for iris-filtered laser treatment showing the effect on ring formation when distance between the iris and the sample is 2 cm (top row) and 25 cm (bottom row), respectively.

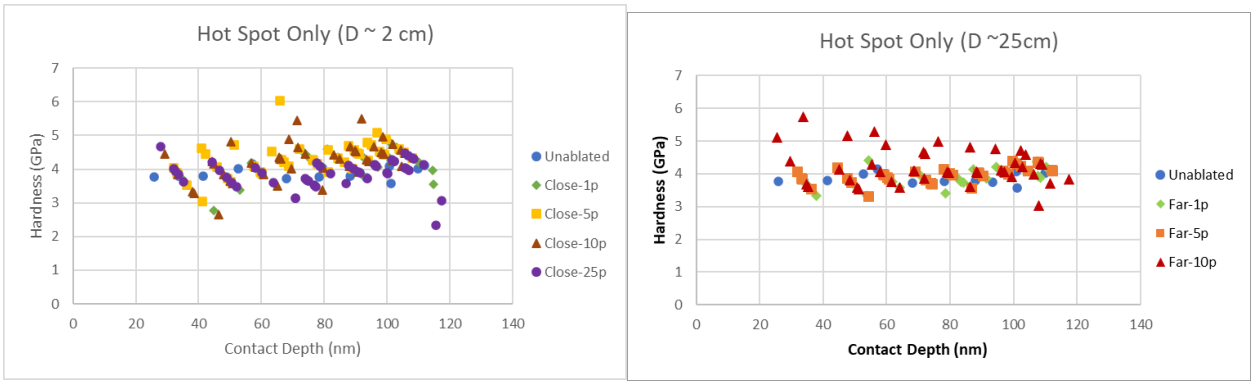

Figure 56. Hardness results for iris-filtered laser treatment with 66 mJ, when the iris is positioned 2 cm and 25 cm from the sample.